The τ-plot, a multicomponent 1-D pole figure plot, to quantify the heterogeneity of plastic deformation

T. H. Simm[a], Y. B. Das[b,c], A. N. Forsey[b], S. Gungor[b], M. E. Fitzpatrick[d], D. G. L. Prakash[a], R. J. Moat[b], S. Birosca[a], J. Quinta da Fonseca[e], K. M. Perkins[a]*

(a) College of Engineering, Swansea University, Bay Campus, Swansea SA1 8EN, UK;

(b) Materials Engineering, The Open University, Walton Hall, Milton Keynes MK7 6AA, UK;

(c) Department of Material Science and Engineering, KTH Royal Institute of Technology, Stockholm SE-10044, Sweden;

(d) Faculty of Engineering, Environment, and Computing, Coventry University, Priory Street, Coventry CV1 5FB, UK

(e) Materials Science Centre, Manchester University, Manchester, UK

* thomas.simm@gmail.com

***Keywords**: TRIP steel; digital image correlation; electron backscatter diffraction; neutron diffraction; diffraction peak profile analysis; planar faults*

Abstract

An approach is presented that allows multi-scale characterisations of heterogeneous deformation in crystalline materials by employing a range of characterisation techniques including: electron backscatter diffraction, digital image correlation and neutron diffraction powder measurements. The approach will be used to obtain critical information about the variations in parameters that characterise the deformed state in different crystallographic orientation texture components of a sample in a statistically significant way. These parameters include lattice strains, texture evolution, peak broadening, dislocation density, planar faults, phase changes and surface strain. This approach allows verification of models of plastic deformation to provide a more detailed view of plastic deformation heterogeneity at multiple length scales than obtained by other characterisation approaches. The approach demonstrated here is applied to two stainless steel alloys; an alloy that exhibits phase transformation during deformation and an alloy that remains the same phase all through deformation process.

1 Introduction

Understanding the micromechanics of plastic deformation in metals is a challenging problem, owing to limitations in both the experimental techniques to characterise the deformed state and the models to describe it. A large part of this is because characterisation methods and deformation models are focussed on information at a particular length scale, whereas in reality plastic deformation causes changes to occur over several length scales. These changes can occur from changes across the size of a sample (10^0 m), to changes at the grain scale (10^{-4} m), then to the scale of the atomic spacing (~10^{-10} m). The changes at the smallest length scale, such as dislocations and planar faults, are particularly important as their behaviour governs the changes at the other length scales. However, characterising these changes in a statistically significant manner is rather challenging, and often experimental methods that provide indirect information of their presence are used. This can be problematic as it can require additional interpretation and makes it difficult to compare techniques.

There are two main characterisation methods used to study the deformed microstructure from the nanoscale to the microscale in a statistically significant manner, powder diffraction and electron microscopy using electron backscatter diffraction (EBSD). Neutron diffraction is widely used to study the plastic deformation of metals. There are two main approaches that are generally followed: powder diffraction method and crystallographic texture measurements. In the former, plastic deformation can be quantified by measuring the changes in phase fraction [1], lattice strain [2], and the quantity and arrangement of dislocations [3–5]; whereas the latter gives information about changes in texture [6] of the alloy and orientations of individual phases. The two approaches provide complementary information about plastic deformation but require separate experimental set-ups. The strength of the neutron diffraction approach is that it can provide information over a larger volume of material and over a range of length scales from macro changes in a sample (*e.g.* quantity of different phases), to changes at the nanoscale (*e.g.* dislocation density). However, individual grain deformation micromechanics and microstructure cannot be directly observed, or their changes tracked. In contrast, electron microscopy approach does allow details of individual grain micro-deformation and microstructural information to be obtained and tracked. However, this is at the expense of a smaller measured volume and

information being obtained for a surface only. Electron microscopy is commonly employed to characterise plastic deformation by utilising information via electron backscatter diffraction (EBSD) and digital image correlation (DIC) [7–10]. They can be used to give information about local changes in grain shape and size, different phases, orientation, dislocation density and surface strain. There are, however, problems with these electron microscopy approaches, which lead to difficulty in characterising a sample and applying plasticity models due to: the limited volume sampled, the importance of surrounding grains below the surface on the plastic deformation of a grain, and differences between the deformation of a free surface relative to the bulk of a sample.

These two techniques provide different and complementary information about the plastically deformed state, but the way in which they are combined is limited due to nature of how a measurement is made. Whilst, in EBSD all orientations are measured, a single measurement of a diffraction peak in powder diffraction is the average of many grains with orientations that satisfy Bragg's law. Furthermore, powder diffraction measurements are most often made at one or two distinct directions relative to the sample, i.e. for planes parallel (axial) and perpendicular (transverse) to the loading direction. This powder diffraction setup means that: 1) the orientations studied are limited, 2) it is more difficult to combine with EBSD measurements, and 3) the nature of the heterogeneity of plastic deformation is not fully explored.

This paper presents a way that the two characterization techniques (EBSD and powder diffraction) can be combined, whilst also providing more information for each technique individually. In this work two stainless steel alloys [11,12] are uni-axially deformed and studied to highlight the approach. A 301 grade austenitic stainless steel alloy (SS301), which readily transforms from austenite phase to martensitic phase during plastic deformation [1,7], and a 316 grade stainless steel (SS316) [13,14], which does not show any particular phase transformation. Deformed samples were measured *ex situ* by powder diffraction and electron backscatter diffraction (EBSD), whilst *in situ* measurements were performed using digital image correlation (DIC).

2 Materials and Methods

The alloys used in this study are different grades of austenitic stainless steel. A 301 grade austenitic stainless steel (SS301) with composition 7.12 wt% Ni, 16.98 wt% Cr, 0.381 wt% Cu, 0.311 wt% Mo, 1.057 wt% Mn, 0.48 wt% Si, 0.043 wt% P, Fe balance. A 316 grade austenitic stainless steel (SS316) with composition 18.1 wt% Cr, 12.2 wt% Ni, 3.0 wt% Mo, Fe balance. All samples were heat treated to produce annealed grains of approximately 30 µm and were nominally fully austenitic (approximately 99%) before testing [7]. During plastic deformation the austenite grains in the SS301 sample transform from austenite to martensite.

All experiments were conducted on material deformed in uniaxial tension or compression at room temperature. In this work, the microstructural evolution during deformation was measured using neutron diffraction and scanning electron microscopy. This was accomplished by using three separate experimental procedures: (1) *ex situ* straining followed by neutron diffraction*, (2) ex situ* straining followed by EBSD; and (3) EBSD and backscatter imaging during *in situ* loading for DIC.

2.1 Neutron Diffraction

Neutron diffraction measurements were obtained using time-of-flight diffraction from the high-resolution powder diffractometer (HRPD) at ISIS Chilton, Didcot, UK. This allowed numerous grains to be measured quickly with a high-resolution diffraction pattern ($\frac{\Delta d}{d} \approx 4 \times 10^{-4}$). Samples of approximately 10 mm^3 were placed in the beam and rotated about an axis perpendicular to the beam. Diffraction patterns were obtained from the backscattering detector bank with a range of 2θ (the angle between the incident and scattered wavevectors) between 160° and 176°, and a range of $g = \frac{1}{d}$ (reciprocal of the interplanar spacing) up to 1.5 Å^{-1}.

For the *ex situ* SS301 measurements by neutron diffraction and scanning electron microscopy, the sample dimensions were based on ASTM E8M sub-size specimen dimensions (flat samples), with gauge width and lengths of 6 mm and 25 mm, respectively. Whereas, the SS316 samples were cylinders with diameter of 20 mm and length 20 mm. The SS301 samples were tested by uniaxial tension and the SS316 samples by uniaxial

compression. The S301 sample studied was deformed up to 20% engineering strain and SS316 to 16% engineering strain.

2.2 Scanning Electron Microscopy

The scanning electron microscopy experiments were performed using a Zeiss Supra 55VP field emission gun scanning electron microscope (FEG SEM). These measurements were only done on the SS301 samples.

For the *ex situ* measurements, EBSD measurements were performed before and after the deformation process on the same set of grains using a step size of 0.2 µm and a map size of ~250 µm by 140 µm (see an example map in Appendix A). Seven different tensile samples, cut from different regions of the as-received material were deformed to macroscopic strains of 5, 6, 7, 8, 9 and 10%. Due to the selective nature of EBSD, only a small subset of the total grains in each tensile sample was measured. Different tensile samples were used for each of the applied strains because unloading and reloading TRIP material has been shown to change the transformation kinetics during subsequent loading steps [15].

For imaging during *in situ* loading, a flat dog-bone shaped specimen with a 20 mm gauge length and a 3 mm gauge width was machined. The specimen was ground and polished using the steps in [7,15] and EBSD was done in the region of interest. A gold remodelled speckle pattern was then applied to produce a speckle pattern suitable for use with DIC using SEM images. The specimen was strained using a 4.5 kN ADMET mini-tensile testing machine mounted inside the SEM. The specimen was incrementally strained *in situ* to an applied strain of approximately 10%. At macroscopic strain increments of 2% the test was interrupted to capture three backscattered electron (BSE) images with a size of ~170 µm by 120 µm (see the starting map used, i.e. before applied deformation, in Appendix A), to be used for DIC analysis. DIC analysis was done using the proprietary software DaVis 8.3 produced by LaVision GmbH [16]. Details of the experimental procedure used can be found in references [7,15].

3 Analytical Procedures

3.1 Electron backscatter diffraction (EBSD)

EBSD analysis was done using a Matlab program created by the authors '*dBSDsteel*' [17], which uses the MTEX toolbox version 4.5.3 [18]. The advantage of this approach is that it allows more control of the data analysis than by using commercial software; this includes more details of the link between austenite and martensite phases, incorporation of polycrystalline plasticity models, calculation of Kernel Average Misorientation (KAM), and linkage with strain data from DIC testing.

The EBSD data were smoothed and non-indexed points filled using a spline filter. Grains were identified for boundary misorientations greater than 5°. To remove regions that may be incorrectly indexed, grains with a boundary less than 10 pixels in length were set as unindexed and the grains are recalculated (again using a misorientation greater than 5°). Average values of the KAM, band contrast (BC), and maximum shear strain ($\gamma_{\max}$ see below) were calculated for each grain. For the average KAM and BC averages, individual points were ignored if the value was larger than 500 or 0.1 respectively (no minimum value, particularly relevant for BC, was used).

The orientation relationship between parent austenite grains and the product martensite plates was found using the Kurdjumov-Sachs (K-S) orientation relationship (OR) approximation [19]. Grain-boundary segments of austenite-martensite boundaries were identified as one of the K-S variants if their misorientation was within 5° of the misorientation of that variant. Using this methodology, a martensite plate could be identified by more than one variant. If this was the case, the variant chosen was the one with the longest boundary, or randomly if two variants had the same length boundary. This then allowed a detailed quantification of the martensite within individual austenite grains.

A program developed by the authors called 'OU-*DICE*' (DIC and EBSD), was used for combining DIC and EBSD analysis, alongside 'dBSDsteel' using the same MTEX toolbox. The initial overlay of the two data sources (DIC and EBSD) requires user judgement, based on the position of microstructural features, with the relative scaling defined by the EBSD step size and the pixel size of the backscatter image used for DIC. The DIC data were then mapped

onto the EBSD data point locations. The strain tensor for each EBSD measurement point was calculated by fitting two-dimensional first-order polynomials across a number of vectors, in this case a 3 × 3 array, using a least-squares approach. When using this method for calculating strain, high levels of overlap of the DIC subregions is beneficial for obtaining good strain maps. The other advantage to this method, over other smoothing approaches, is that the size of the sampled region for each strain tensor is clearly defined, which is important information when interpreting strain data close to a grain boundary.

The pixel size for the SEM-DIC images was 37 nm. The differentiation length of the strain field was 20 pixels, which corresponds to 0.74 µm. The analytical procedure also calculates average strain data within a grain. For these average grain strain data, a similar process was applied as with the local data, but instead of a 3 × 3 array of vectors as used for the strain map, all those vectors inside the grain were used. The data were then filtered by subtracting the fitted displacements from the measured displacements for the grain and removing any vectors more than 2 standard deviations from the mean. The fit was performed for a second time without these outliers that would disproportionately affect the least-squares fit. This filtering assumes uniform strain within the grain, but this is generally not the case. Care was taken in setting the threshold value for the filter so that real features were not removed. The vectors that were removed by the filter were primarily those around the grain boundary.

3.2 Diffraction peak profile analysis (DPPA)

Diffraction peak profile analysis (DPPA) of the neutron data was conducted using '*BIGdippa*', a Matlab program created by the authors [5]. This program was used to fit the diffraction peaks to split pseudo-Voigt functions (i.e with different values of full-width and mixing parameter either side of the peak's centre to account for asymmetry).

DPPA uses the full-width at half maximum intensity (alternatively the integral breadth can be used) of a particular diffraction peak (β_{hkl}) to provide information about the nanostructure of a material. This relationship can be expressed as [5,20]:

$$\beta_{hkl} = \frac{1}{D} + f_M g \sqrt{\left(\rho \acute{C}_{hkl}\right)} \quad (1)$$

where, g is the reciprocal of the d-spacing; the first term is the 'size' component which is reciprocal of the crystal size, D; and the next term the strain component, which is related to $f_{M,}$ a measure of the arrangement of dislocations [5,21]; $\acute{C}_{hkl}$ the contrast factor of dislocations [22]; and ρ the dislocation density.

When there are planar faults present in a sample this causes an additional source of broadening. This can be incorporated in Eq. 1 by replacing $\frac{1}{D}$ with $\frac{1}{Deff_{\cdot hkl}}$, using the following formula [3]:

$$\frac{1}{Deff_{\cdot hkl}} = \frac{1}{D} + \frac{(1.5\varphi+\beta)}{a}\varpi_{hkl} \qquad (2)$$

Where, a is the unit cell size; ϖ_{hkl} is a constant for a particular diffraction plane, $\varpi_{111/222}$ = 0.43 and $\varpi_{200/400}$ = 1 is used; φ is the stacking (or deformation) fault probability; and β is the twin probability.

The position of a diffraction peak is also changed by the presence of deformation faults contributing to that peak. The fraction of deformation faults (φ) within a sample can be given from the lattice strains ($\frac{\Delta d_{hkl}}{d_{hkl}}$) of different orders of the same peak as [3–5]:

$$\varphi = \frac{4\pi}{\sqrt{3}(\chi_{111}-\chi_{222})}\left(-\frac{\Delta d_{111}}{d_{111}} + \frac{\Delta d_{222}}{d_{222}}\right) \qquad (3)$$

Where, $\chi_{111} = \frac{1}{4}$, $\chi_{222} = \frac{-1}{8}$, $\chi_{200} = \frac{-1}{2}$, $\chi_{400} = \frac{1}{4}$ [3] is used.

In this work the full-width is plotted at different measurement directions (see Section 3.4). Equation 1 is used to provide a predicted full-width, using a constant crystal size for a given sample. The strain term is allowed to change for different angles of a sample using the methodology described in [14]. Equation 3 is used to determine the planar fault fraction at different angles. These values are then used with Equation 2 and Equation 1 to provide a predicted broadening that incorporates planar faults.

3.3 Crystal Plasticity

In the CPFEM method, the microstructure is represented as a finite element mesh, where each grain is represented as one or more elements [23]. Local constitutive laws are then used to simulate the behaviour. The model used here uses an elasto-viscoplastic mechanical

model and hardening behaviour is modelled using a modified Voce law [23]. This method has been shown to predict with a good degree of accuracy texture evolutions [5] , the average elastic strains in different grain families during plastic straining [2] . For the simulations in this paper, the SS316 sample deformed to 16% applied strain was used. In the model discrete grains were represented by 20 node, isoparametric brick elements each with 8 integration points. The model used an incremental-iterative scheme with small displacement steps up to 16% strain, after this the displacement steps were reversed until the average stress in the sample was zero, to replicate unloading.

The model is used for just the FCC phase, using single crystal elastic properties: S_{11} = 10.66 × 10^{-6}, S_{22} =−4.29 × 10^{-6}, S_{12} = 7.92 × 10^{-6} all in units MPa^{-1}. The plastic deformation parameters were determined by fitting to the macro stress–strain response of SS316 deformed by compression. The parameters used were obtained were an initial hardening rate of 905 MPa, stage IV hardening rate of 173 MPa, an initial slip resistance of 17 MPa, a saturation slip resistance of 160 MPa and the power law hardening of 1.6. A random texture was used, which is a good approximation for SS316.

Taylor model and Schmid factor calculations are done using MTEX [18]. Simulations are done using a random starting texture. All calculations are made just for the FCC phase.

Whilst, SS301 is tested in tension and SS316 in compression simulations are only shown for compression. Although, compression and tension lead to different results they do so in a systematic way. The orientation changes, caused by slip activity, from compression tests lead to opposite orientation changes than due to tension tests. This is shown in Appendix B, where a Taylor model is used to show that a good approximation that can be made is that the ratio of intensities in compression or tension (I_{comp} *or* I_{tens}) to starting intensity (I_0), can be given as $I_{comp} / I_0 \sim I_0 / I_{tens}$ if both have the same strain. In a similar way the lattice strains obtained in compression can be shown to be approximately the negative of those obtained in tension. Although, the engineering strain of the SS316 and SS301 samples are different, their true strain, 0.18 for SS301 and 0.17 is much closer.

3.4 Geometry of the experiment

In order to compare the neutron data with the SEM data, the latter is separated into orientations based on grains with orientations with hkl plane-normals at different angles to the tensile direction. In

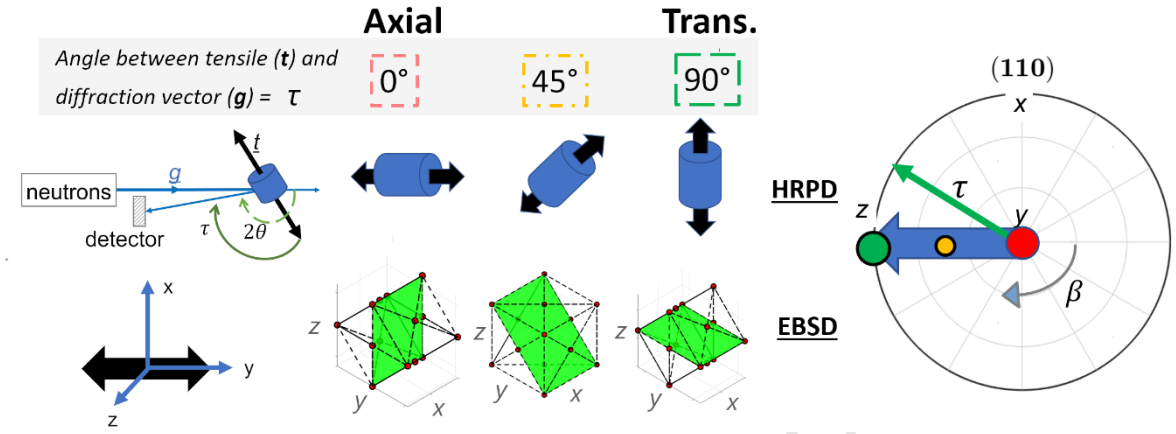

*Figure 1 is a schematic of the experimental and analytical approach used here. In this approach grains are grouped together based on their orientation, and average information about the microstructure of these particular grains is obtained. The orientation of a grain can be defined by the relationship between one of its plane normals (**g** e.g. 111) and a direction in the specimen's geometry. In this approach, grains that have plane normals (**g**) that are parallel the tensile direction (**t**) are grouped together. This is not a unique orientation, since a rotation of a crystal about **g** would give different crystal orientations but would all be grouped together. This experimental methodology is that used in neutron powder diffraction measurements, such as at Engin-X, ISIS, Oxfordshire, where measurements are obtained by two detectors at 90° to each other, to give information parallel to the axial or transverse directions (the red and green circles respectively, in the pole figure of*

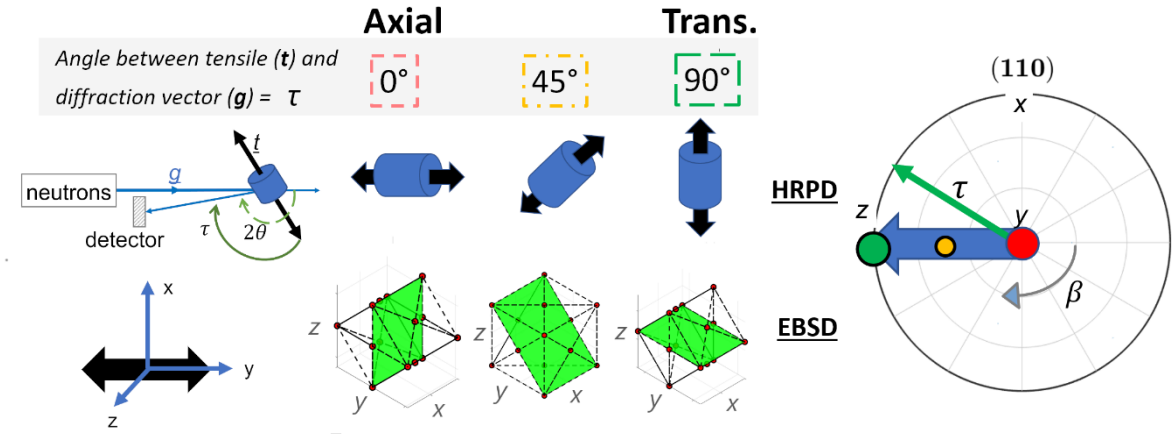

Figure 1). The difference between that approach and the methodology used here is that several angles between the axial and transverse directions are measured (the blue arrow in

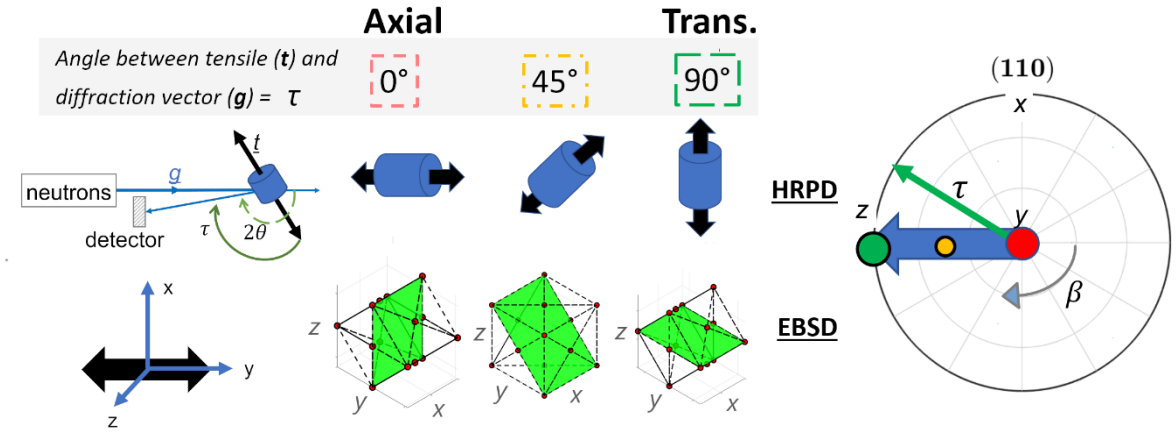

Figure 1). To apply this approach to powder diffraction and electron microscopy measurements requires a slightly different procedure. For the powder diffraction measurements, the samples are rotated (and so the tensile direction ***t*** is also rotated) because the detectors and neutron beam are fixed. Whereas, for electron microscopy, the sample is fixed, and different orientation families are determined from EBSD measurements and the diffraction vector ***g*** is effectively rotated. To do this, orientations are identified that have a *hkl* plane normal within 15° of the vector ***g***. This is not exactly the same as the orientations measured by the neutron diffraction detectors but is a reasonable approximation. A second difference with the procedure used for the SEM measurements is that, unlike the powder diffraction measurements, τ is determined across a range of axes, or angle ϑ in the figure. For powder diffraction the measurements are made between the y-axis and z-axis, whereas for SEM measurements the data is determined by taking the average value from a number of ϑ angles. The reason for the additional averaging in the SEM data is discussed in the results section. The two different procedures (for EBSD and powder diffraction) are comparable, in that grains are being measured with different angles between the tensile direction and diffraction vectors.

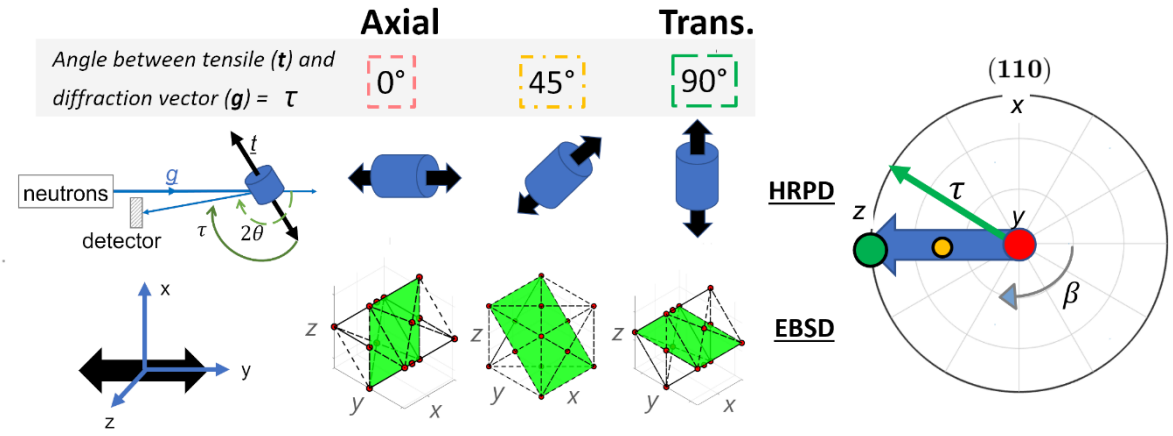

*Figure 1. The geometry of the experimental setup. Measurements are made at angles τ between the tensile/compression vector (**t**) and diffraction vector (**g**) of a particular plane (or it's normal). For neutron measurements using HRPD, the sample is rotated (rotating **t**). Whereas for EBSD measurements, grains with orientations with plane normals at angles between **t** and perpendicular to **t** (z-direction) are evaluated (effectively rotating **g**). Both approaches are taking measurements of τ between two perpendicular directions on a pole figure of a peak (110 is shown as an example), or between the centre and outside of the pole figure.*

4 Results

The first part of the results section looks at how information about the plastically deformed state can be obtained from microstructural observations and averaged values. This is then

used for comparison with the τ plots which are presented in the final parts of the results section. Hence, allowing assessment of these τ plots to study the plastically deformed state.

4.1 Microstructure

4.1.1 SEM Microstructural Observations

For SS301, with increased amounts of plastic deformation more martensite is formed. This change is shown in

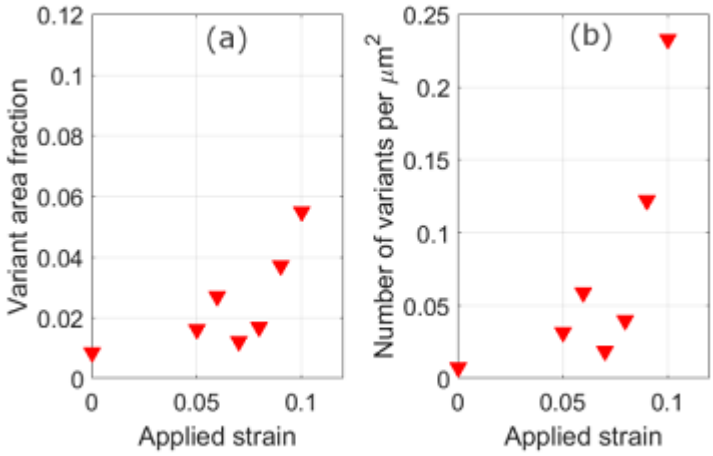

Figure 2 using EBSD measurements. The amount of martensite is relatively unchanged until before 9% applied strain. After 10% applied strain the martensite area fraction is ~6%. These changes are slightly different to those found by powder diffraction [1], where the volume fractions are slightly higher and changes are more gradual. They are shown here to give an indication of the errors involved in quantifying martensite in later sections.

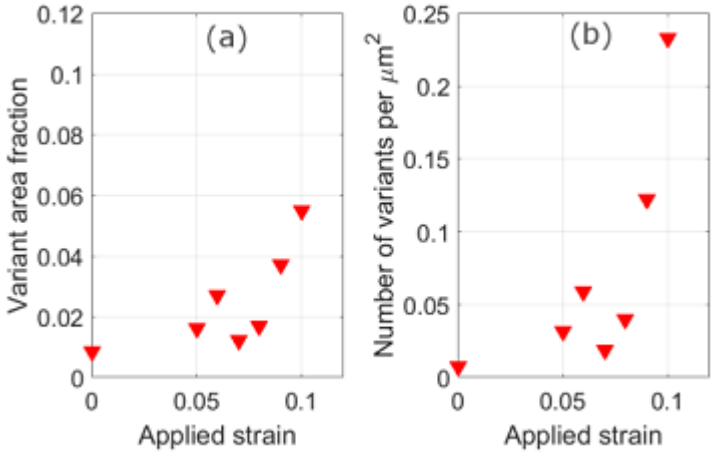

Figure 2.The change in the fraction of martensite with applied strain of SS301. (a) the area fraction from ex situ *EBSD measurements, (b) the number of variants per μm^2 from ex situ EBSD measurements.*

The relationship between strain and orientation changes at the microstructural scale can be examined by considering EBSD orientation and DIC strain data. Figure 3 shows EBSD plots of a selected region from the *in situ* DIC test before testing (0% strain) and after 10% applied strain. After deformation, the region consists of several austenite grains, some of which are grains that contain a significant amount of deformation-induced martensite (*e.g.* grains '*a*' and '*b*'), some that consist of no martensite (e.g. grains '*d*', '*e*' and '*g*'), and some grains with a very small amount of martensite (e.g. grains '*c*' and '*f*'). The figure shows Kernel Average Misorientation (KAM) and misorientation from mean (or grain orientation spread GOS) calculated using EBSD, maximum shear strain measured by DIC ($\gamma_{\max}$), and the band contrast (BC), which reflects the quality of EBSD kikuchi patterns and, in a similar manner to peak broadening in DPPA, gives an indication of the dislocation density.

Clearly, there is not a good correlation at the microstructural scale between EBSD and DIC measurements. For example, there are regions of high maximum shear strain within some grains and these regions do not in turn correspond to regions of high local misorientation (KAM). Instead, regions of high KAM are mainly concentrated around grain boundaries, which in some cases correspond to regions of higher strain, but not always. The same lack of correlation is also found when comparing GOS and maximum shear strain maps. The band contrast maps show slip lines seen in the DIC map (such as in grain '*1*' with a lower value of band contrast) but these are not visible in the KAM maps. In addition, regions of high KAM density (e.g. the bottom of grain '6', or in grain '*7*') do not correspond to regions of lower band contrast. A secondary problem with the KAM and band contrast maps that is highlighted in Figure 3, is the influence of sample preparation. The post-test EBSD maps were necessarily prepared after testing, and so to ensure the same region was measured they were lightly polished by an OPS solution. However, this simplified EBSD sample preparation introduces some surface scratches, which cannot be removed during the gentle polishing process. The influence of sample preparation is one of the main problems with KAM maps, but much less of a problem with maps that plot the misorientation relative to the mean (GOS).

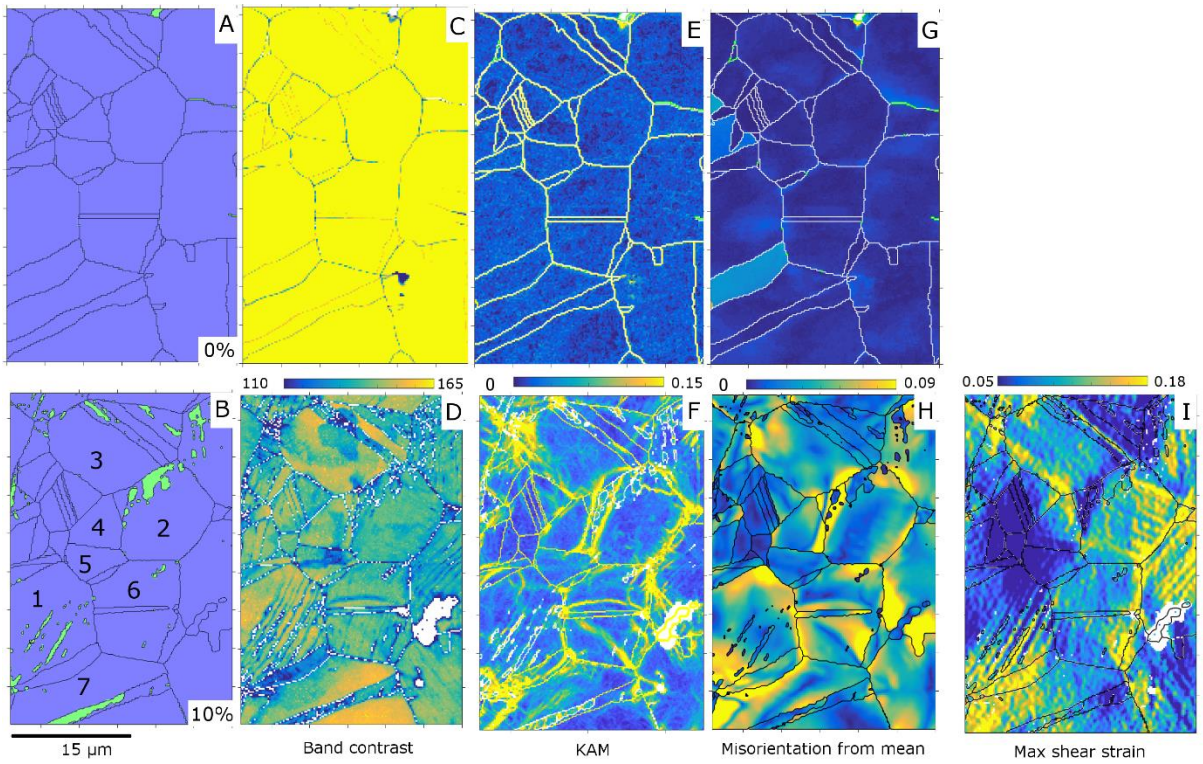

Figure 3. EBSD plots before testing (%) and after 10% applied strain from selected region. Subfigures A and B show a phase map, subfigures C and D are band contrast maps, subfigures E and F are the plots of KAM, subfigures G and H are maps of the misorientation angle from the mean orientation of a grain, and in subfigure I the maximum shear strain from DIC. The top subfigures (A, C, E, G) show the sample before testing, and in the bottom subfigures (B, D, F, H, I) after testing to 10% applied strain. Selected grains labelled 1-7 have been highlighted in B. In the band contrast plot the white pixels are non-indexed points, these are cleaned by a spline filter for the other plots.

4.1.2 SEM Averaged Values

At the microstructural scale, the relationship between the different measured variables is weak. However, this does not mean that there is no link between the variables. When averaged across the whole sample, all of these variables increase (or decrease in the case of BC) with increasing applied strain, as would be expected. The relationship between the variables at the grain scale can be examined by considering the averaged values in different grains. This is done in Figure 4 which shows a scatter plot of the average values of Kernel Average Misorientation, KAM, against the averaged maximum shear strain (γ_{max}) and averaged reciprocal of the band contrast (note higher band contrast corresponds to less deformation). This figure shows there is a relationship between KAM with both the BC and maximum shear strain (γ_{max}) in grains. To quantify this relationship more rigorously, the Pearson correlation coefficient, or *r* is used, with the results shown in Table 1 and Appendix C. The Pearson correlation coefficient is a method of determining if there is a relationship between two variables [24], which is given as: 0.00-0.19 very weak; 0.20-0.39 weak; 0.40-

0.59 moderate; 0.60-0.79 strong; 0.80-1.00 very strong [25]. Although, the method has limitations it is only used here as a guide. Furthermore, the values discussed for 10% shown in Table 1 are comparable to those observed for different strains shown in Appendix C. Note the values for comparisons with DIC data are less statistically significant, this is because the map size is smaller. But is also because the same region is used at different applied strains, which is not the case for the KAM and BC data, hence why only the values for 10% strain are shown.

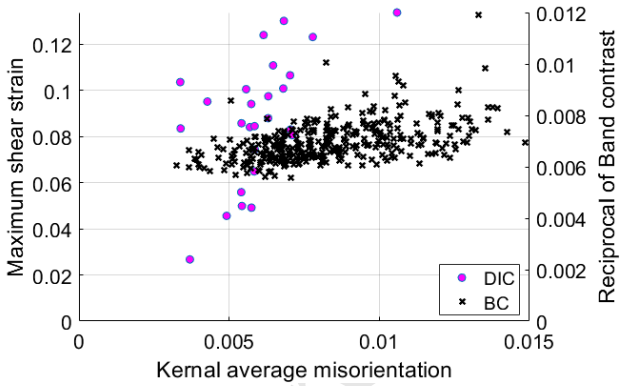

Figure 4. Scatter plots showing the average kernel average misorientation in different grains plotted against their average maximum shear strain γ_{max} (DIC) and the reciprocal of their average band contrast (BC). The data is for SS301 after 10% applied strain, the DIC data uses a higher magnification (and lower area) map than the BC data.

Table 1. The Pearson correlation coefficient for the grain averaged values of different variables. The data is for SS301 after 10% applied strain, the DIC data uses a higher magnification (and lower area) map than the BC and KAM data. For the band contrast values, its reciprocal is used. See Appendix C for data at 9% and 8% applied strain. The DIC data uses the low magnification map (170 x 120 µm) followed by the high magnification map (70 x 42 µm) for comparisons with the Taylor and Schmid factor, and just the high magnification map for comparison with BC and KAM.

	DIC	KAM	BC	TF	SF
Max shear strain γ_{max} (DIC)	-				
KAM	0.54	-			
BC	0.15	0.55	-		
Taylor Factor (TF)	-0.05 / -0.33	0.15	0.33	-	
Max. Schmid Factor (SF)	0.26 / 0.57	-0.04	-0.15	-0.66	-

The table shows there is a moderate correlation between KAM and BC, which can also be seen from the values in the appendix. In addition, there is a moderate correlation between KAM and maximum shear strain; but a very weak correlation between BC and maximum shear strain. Therefore, as may be expected there is some correlation between all the different measures of plastic deformation studied at the grain scale, but because they represent different details of plastic deformation the correlation is not strong.

The Taylor factor and Schmid factor are parameters obtained from polycrystal plasticity methods that are often used to determine differences in plastic deformation [7,8,26,27]. Table 1 shows that the Schmid factor has a moderate correlation with the maximum shear strain, but a very weak and inverse relationship with KAM and BC. Conversely, the Taylor factor has a weak inverse relationship with the maximum shear strain (i.e. correlation between grains with high Taylor factor and low max. shear strain), but a weak and very weak relationship with BC and KAM respectively.

4.2 The τ plot

A way to try to understand and quantify differences in the deformation of different grains is to group grains together based on their orientation in the way shown in Section 3.4 and

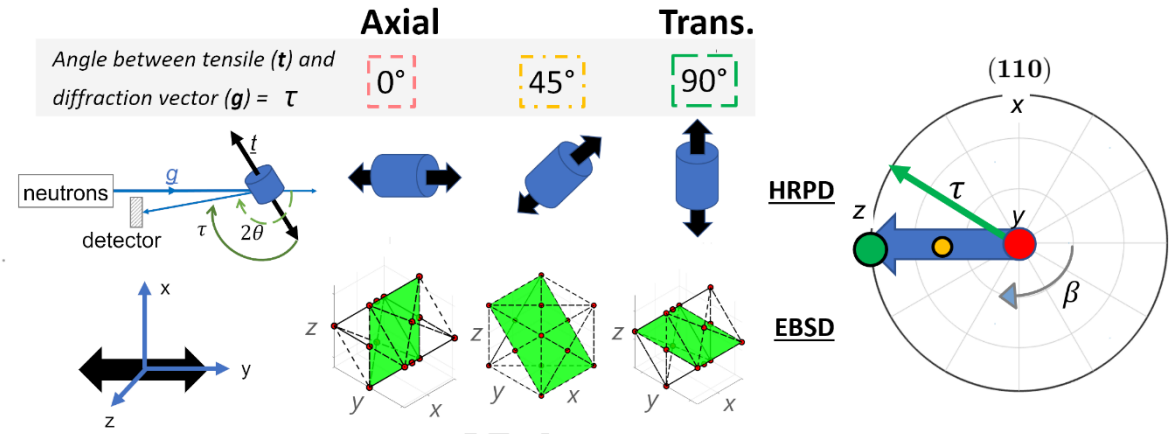

Figure 1. The plot can be used with both powder diffraction measurements (Section 4.2.1) and SEM measurements (Section 4.2.2). Hence, in turn offers a way to combine SEM and powder diffraction data.

4.2.1 Powder Diffraction Measurements

From the powder diffraction measurements three main parameters are obtained: lattice strains, peak intensity, and diffraction peak broadening from the full-width at half maximum intensity (full-width). The measured values for these parameters at different angles between tensile and diffraction vectors, or τ, for planes *111*, *200* and *220* are shown in Figure 5 for SS301 and SS316 specimens. Each of these parameters can be predicted using polycrystal plasticity models. Note to account for SS301 being in compression (see Section 3.3) that the negative of the lattice strains and the inverse of the intensity change ratio is plotted for SS301. In this case a crystal plasticity finite element model (CPFEM) was employed to highlight this, with the results shown alongside the measured values.

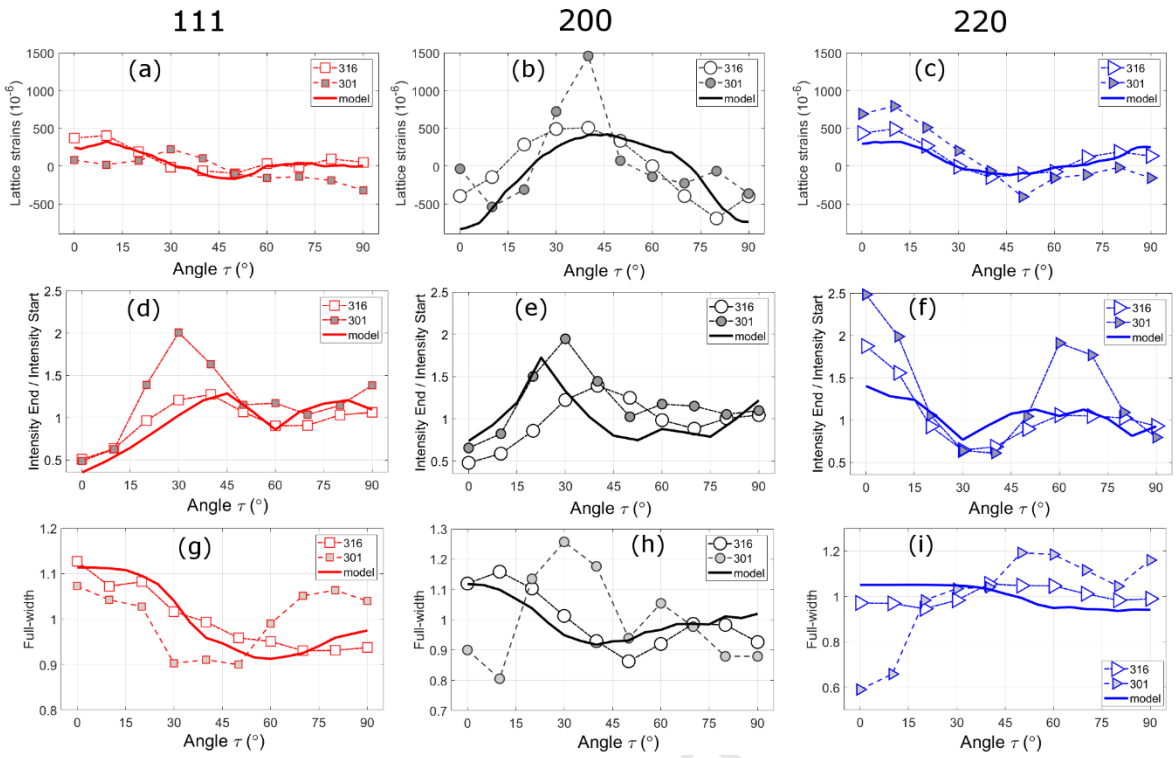

Figure 5. The measured and predicted lattice strains (a-c), intensity change (d-f), and full-width (g-i) with angle between tensile and diffraction vectors τ, for planes 111 (a, d, g), 200 (b, e, h) and 220 (c, f, i). The data is plotted for SS316 deformed to 16% applied strain and SS301 deformed to 20% applied strain, both at room-temperature. The models data is calculated using CPFEM [23]*. The full-width values are calculated using equal edge and screw dislocations and the same micro-strain and crystal size values for all three peak (more details on the method are in* [14]*). Values of full-width are arbitrary normalised values to highlight changes with angle. The 111 lattice strain is determined from the 111 and 222 lattice strains using a rearrangement of Eq. 3 to determine a lattice strain with no planar fault contribution (i.e. almost an average of the 111 and 222 lattice strains). The same is done for the 200 peak using the 200 and 400 values.*

Most research measurements of lattice strains due to tensile tests are done on samples that are loaded. However, as shown in Figure 5, there are still lattice strains present in the alloys after unloading. The magnitudes of these strains are of a similar order to those observed in the transverse direction of an SS301 sample when loaded at room-temperature, as shown in Appendix D. For example, when the SS301 sample is loaded to an applied strain of 20%, the lattice strains in the axial direction varied from 6000 x 10^{-6} for the *200* peak to 2000 x 10^{-6} for the *220* peak, and between -1000 x 10^{-6} for the *200* peak and -700 x 10^{-6} for *220* peak in the transverse direction. Although the changes in lattice strains in Figure 5 are relatively small, clear trends can be observed for the two alloys and three observed peaks. Furthermore, there are similarities between the behaviour of the individual peaks for the two alloys, and the SS316 results are close to the CPFEM predictions. For example, *111* has lower lattice strains than the others, for *200* lattice strains start negative ($\tau = 0°$) increase to a maximum ($\tau = 45°$) then fall to a negative value ($\tau = 90°$). Moreover, for the *220* peak the

lattice strain starts at a high positive value ($\tau = 0°$) falls to a negative value smaller in magnitude ($\tau = 45°$) and then increases to a positive value ($\tau = 90°$).

There can be problems with determining the lattice strains in alloys such as SS301 where transformation from austenite to martensite occurs [1]. This is due to three reasons. Firstly, there may be different carbon contents in different grains. Differences in carbon content will lead to differences in lattice spacing and the carbon content will influence the ease with which martensite forms. Secondly, the stresses will vary from grain to grain causing a range of lattice spacings, but martensite formation may occur preferentially in grains with higher stress. Finally, these alloys can have a high content of planar faults and as shown in Eq. 3 planar faults can cause shifts in the peaks. Given these issues and that SS316 is used for the CPFEM, it is interesting to find that the lattice strains of SS301 are relatively close to those observed for SS316.

The graphs in the middle row in Figure 5 show the changes in peak intensity with angle τ for *111*, *200* and *220* peaks. The intensity at the end divided by the starting intensity is plotted for SS316 and the model predictions, such that a value more than 1 means an increase in grains having that orientation, and a value less than 1 a decrease in grains having that orientation (1 means no change in texture). Whereas, for SS301 the intensity at the start divided by the starting intensity is plotted (because SS301 is tested in tension whereas SS316 and the model are tested in compression). The changes for SS316 and SS301 are close to each other and the FE model predictions, for example: (1) For *111* the intensity-change predicted and measured SS316 values are less than 1 at $\tau = 0°$, increase to a maximum at $\tau = 40°$ and then fall before an increase to $\tau = 90°$. (2) For *200*, the SS316 measured intensity-change values are similar to those found for *111*, the predicted *200* values show similarities with the measured values, but the position of the maximum value (and the overall changes) are notably different, being shifted to a lower angle (23° and 37°). (3) For *220* the intensity-change SS316 measured values are the opposite of those seen for *111* and *200*, that is maximum value on the *220* plot is close to a minimum on the others (and vice versa). These changes are also reflected in the *220* predictions, which are close to the measured values. There are some differences between SS301 and SS316, these differences are used to make an estimate of which grains transform in a later section.

The use of polycrystal plasticity models to predict diffraction peak broadening [4,14,28,29] is a less developed modelling route than for texture or lattice strains. In this method a polycrystal plasticity model is used to predict the activity of different slip systems in different grains, this is converted to broadening by an assumption on the relationship between slip activity and dislocation density. The broadening is then found by incorporating the contrast factor of dislocations, which adjusts for differences in the strain field of dislocations caused by the angle between their Burgers vector, plane normal relative to the diffraction vector. The modelling of the full-width of SS316 in this way, and its limitations, is dealt with in more detail elsewhere [4]. The changes for SS316 are close to the FE model predictions, for example: (1) an overall fall in full-width for *111* and *200* peaks between τ = *0°* and τ = *90°*, (2) a minimum in full-width for *111* and *200* peaks at an angle in the middle, and at a lower angle for the *200* peak (although the minimum for the *111* peak is only just noticeable in the measured data). (3) the smaller relative changes in full-width of the *200* peak. However, predictions and measurements do show noticeable differences, which is probably due to the simplicity of the approach in describing dislocation dynamics and the resulting deformation microstructure. The full-width values of SS301 are markedly different to SS316 for the *200* and *220* peaks, and less so for the *111* peak.

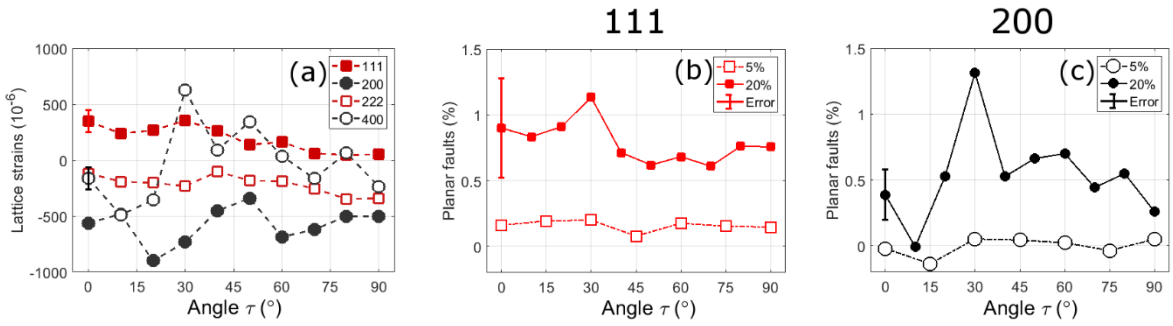

Figure 6. Plots of the change of lattice strains of the SS301 sample deformed to 20% applied strain with τ for 111 and 222 reflections, and 200 and 400 reflections are shown in (a). In (b) and (c) are planar fault values determined from the lattice strains using Eq. 3. This is done for (b) 111 and (c) 200 peaks for 5% and 20% applied strain samples. The error bars are based on $\Delta d/d=100x10^{-6}$.

For the SS301 sample at 20% applied strain, there is a marked difference in the lattice strains of the different orders (Figure 6), which would not be expected from CPFEM strain predictions (see also [4]). The lattice strains for the *111* and *200* peaks and the higher order *222* and *400* peaks are shown in Figure 6a for the 20% strained SS301 sample using the τ plots. As shown by Eq. 3, this difference in lattice strains can be caused by the presence of

planar faults. Using this equation, the fault percentages with angle τ for the *111* and *200* peaks are shown in Figure 6b-c. The planar fault percentage at 20% applied strain has a maximum of ~1.4% and varies significantly with orientation. This is most notable for the *200* peak which has a clear maximum at ~30°. The planar fault percentage is more constant for the *111* peak but also has a maxima at ~30°, although it is worth noting the error is twice that of *200* due to χ values (used in Eq. 3). For the 5% SS301 sample and the SS316 samples, the difference in lattice strains is much smaller and almost constant across angles. For example for SS316 at 16%, there is a planar fault percentage of 0.19% for *111*/*222* and -0.15% for *200*/*400* (i.e. the movement of *200* relative to *400* is the opposite of that expected for planar faults) [4]. Although the CPFEM model used here does not predict martensite (and indeed planar fault) formation, this type of experiment could be a useful approach to verify models that do.

4.2.2 SEM Measurements

The EBSD maps used in this work are typical in size for what may be used for microstructural observations (see Appendix A). However, they represent a much smaller area than would be used for standard (intensity) pole figures, and sample a much smaller volume than obtained by the neutron measurements. To investigate how representative these maps are, pole figures for the *200* peak at 8%, 9%, and 10% are shown in Figure 7. It would be expected that the pole figures would be similar but display a gradually changing texture with increased strain if they were representative. This is not what is observed, instead the positions of maximum intensity move around between pole figures. This suggests the area used in the maps is too small for standard pole figure plots.

In Figure 8 these pole figures are reduced to one dimension by taking the average intensity at different distances to the centre, the τ plot. To account for the starting texture and to compare with the neutron measurements (also shown in the figure) the ratios of the final and starting intensities are shown. The τ plots of intensity from the SEM measurements at different applied strains are close to each other, as would be expected given the small differences in strain between samples. Note that if the intensity is integrated along an arbitrary line from z to the pole figures edge in Figure 7, such as from z to x, the changes in intensity would be very different between different samples. Hence, the justification for integrating from the tensile direction (z) to all angles perpendicular to this (the edges of the

circle). From Figure 8 it can also be seen that there is a good correlation between the SEM and powder diffraction measurements for each of the peaks. Hence, these observations give justification that the use of the τ plots with the SEM measurements are characteristic of the samples. Although, if texture changes alone were of interest this approach is not the best available.

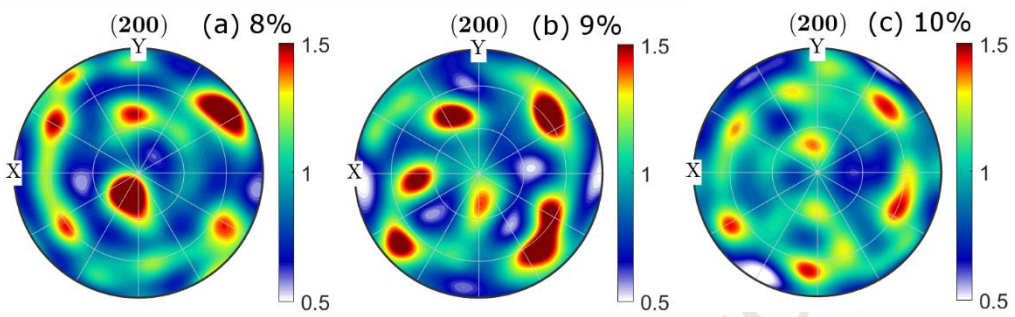

Figure 7. Pole figures for the 200 peak of SS301 after (a) 8%, (b) 9%, and (c) 10% applied strain. The tensile direction is the z-direction and τ is 0° at the centre and 90° at the circle's edge.

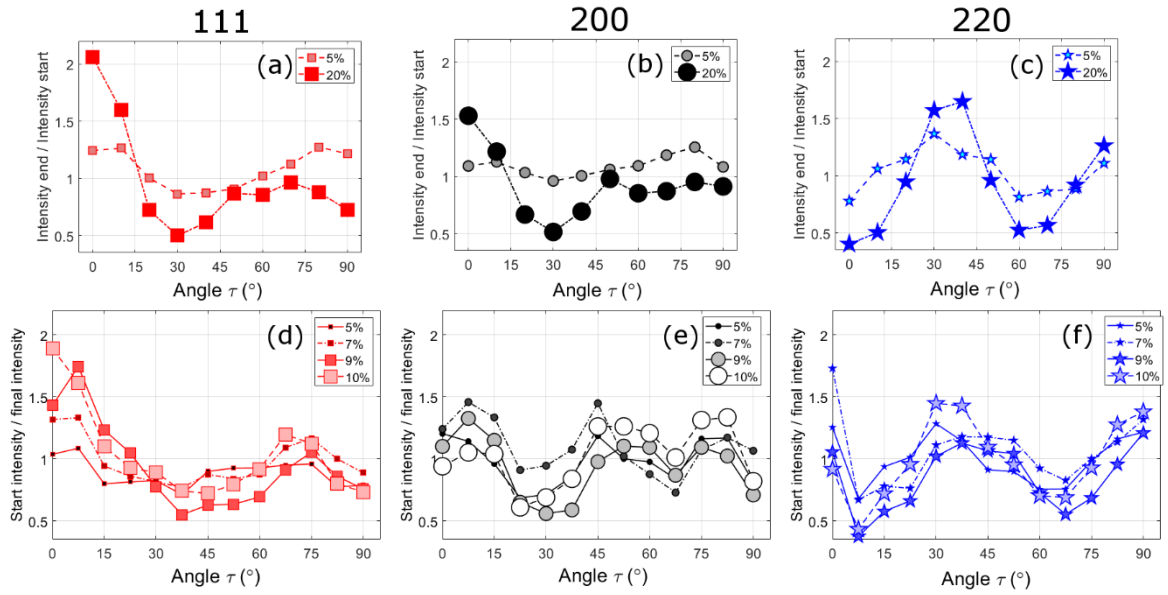

Figure 8. The ratio of starting and final intensities of SS301 using powder diffraction data (a-c) and EBSD data (d-f). This is done using the τ plots for 111 (a, d), 200 (b, e) and 220 (c, f) peaks.

Using EBSD orientation measurements, martensite grains are merged with 'parent' austenite grains if they are within a tolerance to a Kurdjumov-Sachs orientation relationship. This allows quantification of the amount of martensite in each FCC grain. For a particular value of τ the area of the martensite daughters divided by the merged parent grains area (including

FCC and BCC components) is obtained and shown in

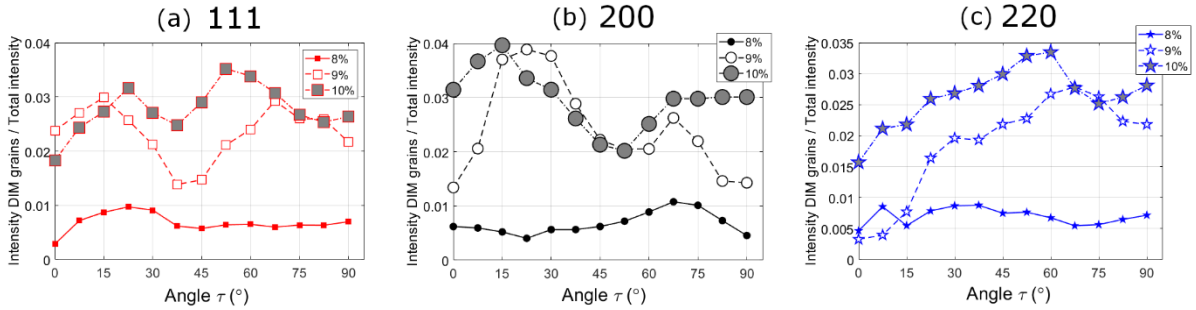

Figure 9. In the figure a large value represents more grains of that orientation family having transformed to martensite. The values vary significantly, by more than a factor of 2, with τ for the different peaks. For example, for *111* there are maxima at τ~20° and 60° and minima at τ~45°, for *200* there is a maxima at τ~20° and a minima at τ~55°, and for *220* a maxima at τ~60° and minima at τ~0°. It is also notable that the positions of maxima and minima are similar for 9% and 10%, which suggests that the behaviour are those observed rather than artefacts.

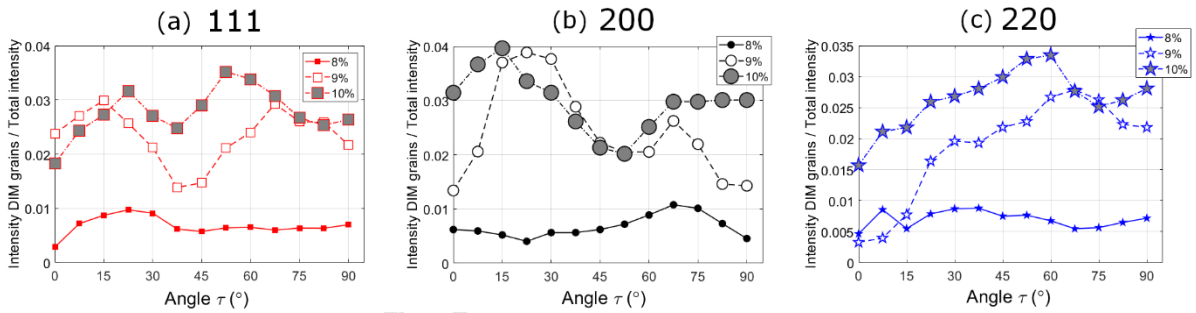

Figure 9. Figures showing the ratio of the area of martensite relative to the area of the combined austenite-martensite merged grain, see text for how this is calculated. This is done for different angles between tensile and diffraction vectors τ, for planes 111 (a), 200 (b) and 220 (c). The values are obtained using EBSD maps of SS301 samples deformed to 8%, 9% and 10% applied strain. A higher value indicates that more grains of this orientation contains martensite.

From EBSD measurements, several parameters can be obtained that are related to the dislocation density: (1) the band contrast (BC), (2) the band slope, (3) the kernel average misorientation (KAM), and (4) the geometrically necessary

dislocation density. The first two and last two are closely related, so only one KAM is plotted in

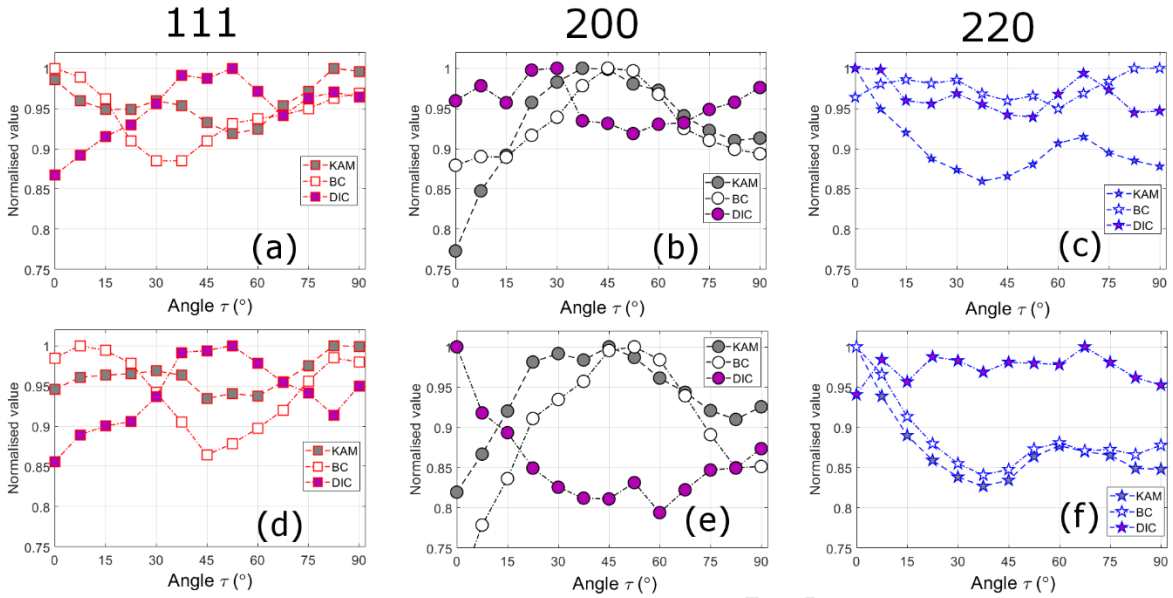

Figure 10. In the figure these τ plots are plotted for SS301 after 5% and 10% applied strain for 111, 200 and 220 peaks. The measures of plastic deformation shown in

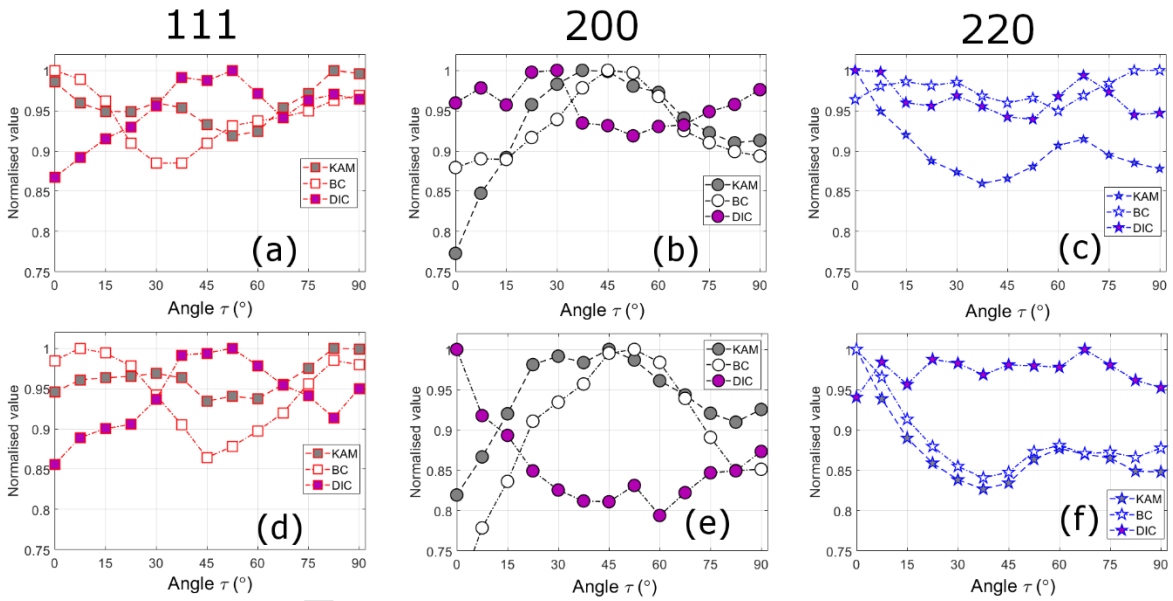

Figure 10 vary significantly, by up to 30%, for different families of orientations (or values of τ for different *hkl* peaks). The changes at the different strains are very similar. It can also be seen in the figure that the KAM and BC values show similar behaviour. However, this behaviour is not observed for the DIC strain data, as shown for the *200* and *220* peaks. This observation is unusual given the correlation relationships shown in Table 1. For example, for *111* there are maxima at τ~0° and 90° and minima at τ~45°, for *200* there is a maxima at τ~45° and a minima at τ~0° and τ~90°, and for 220 a maxima at τ~0° and τ~60° and minima at τ~40°.

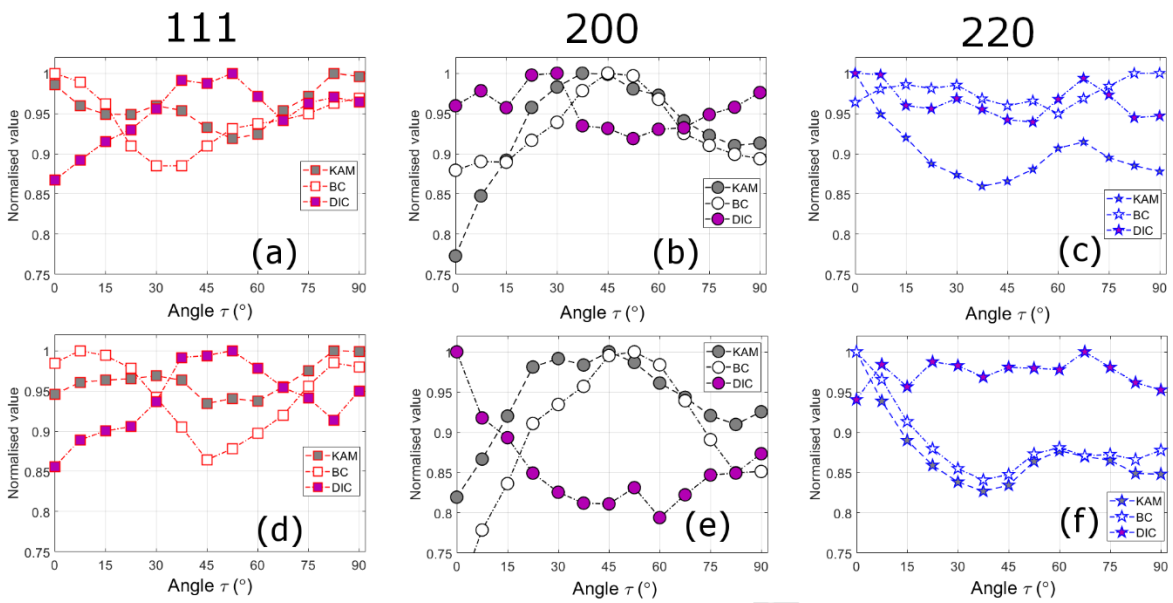

Figure 10. The change in measures of plastic deformation from SEM measurements with angle between tensile and diffraction vectors τ, for planes 111 (a, d), 200 (b, e) and 220 (c, f). The average kernal average misorientation (KAM), band contrast (BC) and maximum shear strain from DIC (DIC) are shown. In the top plots (a, b, c) are for values from a sample deformed to 5% applied strain, and in the bottom plots (d, e, f) show values from a sample deformed to 10% applied strain.

5 Discussion

The use of the τ plots with powder diffraction data is a useful way to verify, or otherwise, models of the crystal plasticity of alloys. It has the advantage of providing several parameters that change due to plastic deformation, which exist across several length scales: lattice strains, texture changes, dislocation density and arrangement, and planar faults. It does this in a way that highlights and can be used to quantify the heterogeneity of deformation. However, these measurements on their own without additional modelling are limited in their use in understanding the deformation of an alloy. In contrast, SEM measurements provide details of deformation at microstructural scale, such as the location of orientation gradients (and hence details of the dislocation arrangement) and deformation induced martensite. However, due to the smaller volume sampled the information they provide is statistically less significant. In this section it is shown how the powder diffraction and SEM measurements can be combined using the τ plots. This is done for the amount of deformation induced martensite and plastic deformation.

It will also be investigated whether these changes can be linked to polycrystal plasticity models. The Schmid factor and Taylor factor are variables that can be used to quantify how much deformation a grain undergoes. Grains with larger Schmid factors or Taylor factors

may be expected to undergo more deformation. The larger the Schmid factor is for a given grain and slip system, the greater the resolved shear stress and hence the easier a slip system is to activate. Hence, if it is assumed that all grains in a polycrystal have the same stress, or they can be treated as single crystals, then the activity of the slip systems could be given by the Schmid factor. Conversely, the Taylor factor is determined from a model (the Taylor model [30]) that assumes that all grains have the same strain as the imposed strain. The Taylor factor of an individual grain is the sum of the activity of the slip systems found by the model. Hence, if there is a direct relationship between slip activity and dislocation density, then grains with higher Taylor factors would have higher dislocation densities.

5.1 Martensite and Planar Faults

It has been shown how details of the deformation induced martensite can be obtained by SEM measurements; including their microstructure and position, and their quantity in different orientations using the τ plots. In contrast, neutron measurements cannot be used to obtain either microstructural details or the amount of martensite in different orientations by directly using the τ plots. The reason that powder diffraction intensity measurements cannot be used to quantify the amount of martensite is due to the significant orientation changes caused by slip, as shown by the changes of intensity of SS316. However, an approximation can be made by comparing the intensity changes of the SS301 and SS316 samples.

Firstly, we can say that if intensity change is only due to slip then $I_{316} / I_0 \sim I_0 / I_{301}$ for the SS301 20% and SS316 16% samples, explained in Section 3.3 and Appendix B. Secondly, we say that the intensity of a given grain can be given by a change in orientation caused by slip (ΔI^{slip}) and martensite (ΔI^{mart}) relative to a starting intensity (I_0). Then the intensity at a given value of τ can be approximated as:

$$I(\tau) = I_0 + \Delta I^{slip} + \Delta I^{mart}, \text{ or } \frac{I}{I_0} = 1 + \frac{\Delta I^{slip}}{I_0} + \frac{\Delta I^{mart}}{I_0} \quad (4)$$

Assuming the intensity of SS316 changes only due to slip, the ratio of its intensity before (I_0^{316}) after deformation (I^{316}) are given by:

$$1 + \frac{\Delta I^{slip}}{I_0} = \frac{I^{316}}{I_0^{316}}$$

Then, if we assume orientation change due to slip is the same in both SS301 and SS316, the orientation change by martensite in SS301 (ΔI^{mart}) can be given by combining the two equations:

$$\frac{\Delta I^{mart}}{I_0} = \frac{I^{301}}{I_0^{301}} - \frac{I^{316}}{I_0^{316}}, \text{ or } \frac{I^{mart}}{I_0} = 1 + \frac{I^{301}}{I_0^{301}} - \frac{I^{316}}{I_0^{316}} \quad (5)$$

where the ratio of the intensity of SS301 before after deformation are I_0^{301} and I^{301} respectively.

In Figure 11 the predicted value of I_{comp} / I_0 for SS301 is plotted using the above equation. A small value in the figure indicates more transformation, since transformation lower the intensity of the FCC grain (N.B. the y-axis in the figure is reversed). The figure shows significant changes in values with τ that are slightly different for each peak. In the figure, the quantity of martensite determined by SEM measurements is also shown. The changes in the amount of martensite with τ on these plots is similar for the two techniques; recalling that a maximum in the SEM measurements corresponds to a minimum in the powder measurements, with both corresponding to more martensite. For example, the minima/maxima (more martensite) at ~30° and ~60° for the *111* peak, ~25° for the *200* peak and ~65° for the *220* peak.

In the same figure the planar faults, determined from the lattice strains using the powder diffraction measurements, are also shown. There is also a similarity in the position of the planar fault maxima with those found for the martensite maxima in previous figures. The large errors in determining the planar fault percentage must be considered and may be the reason that the planar fault and martensite changes are slightly different. It has been proposed that there is a link between planar faults and martensite formation [1], which would be consistent with the results shown here. However, this relationship can be difficult to verify experimentally in a statistically significant way as shown here.

It was previously shown using DIC strain data [7], that the majority of grains in SS301 deform principally by single slip and that the active slip system in a grain is often given by the one with the highest Schmid factor. Furthermore, the formation of martensite was also found to be linked to this behaviour, with martensite laths forming along FCC planes with high Schmid factor. Hence, the approximation of treating grains as a single crystal as done with

the Schmid factor (or Sachs model [31]) may be a reasonable approximation for grains in this alloy in some cases. To investigate this relationship, the change in the maximum Schmid factor has also been plotted on the τ plots in Figure 11. The changes in the Schmid factor for *200* and *220* τ plots are similar to the changes in martensite and planar fault changes. However, the changes in the Schmid factor for the *111* peak is noticeably different to the changes in martensite and planar fault changes. The difference is mainly due to the presence of a minimum at ~45° that is present in the martensite/planar fault values but not the Schmid factors. This suggests there is a reasonable relationship between planar fault and martensite formation with the Schmid factor, but that it is not the only consideration.

If the changes in surface strain (DIC) in

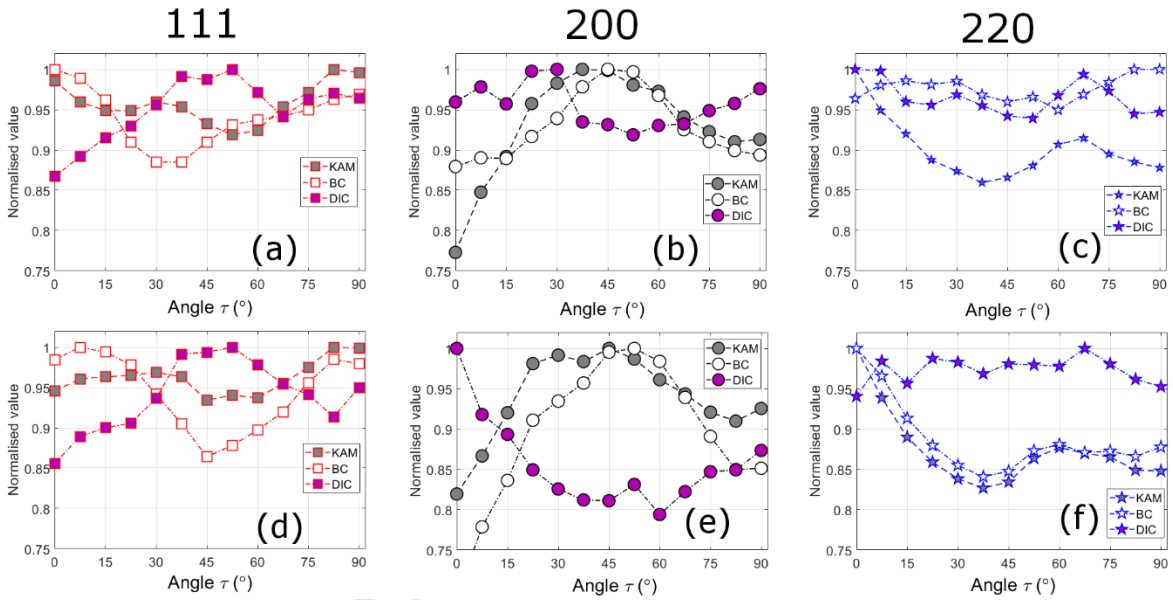

Figure 10 are compared to the changes in Figure 11 it can be seen that there is a good correlation with the changes in the τ plots. So this provides evidence for the link proposed in [7] of a link between the Schmid factor and both martensite formation and surface strain. Whilst extending this to also include a link with stacking faults.

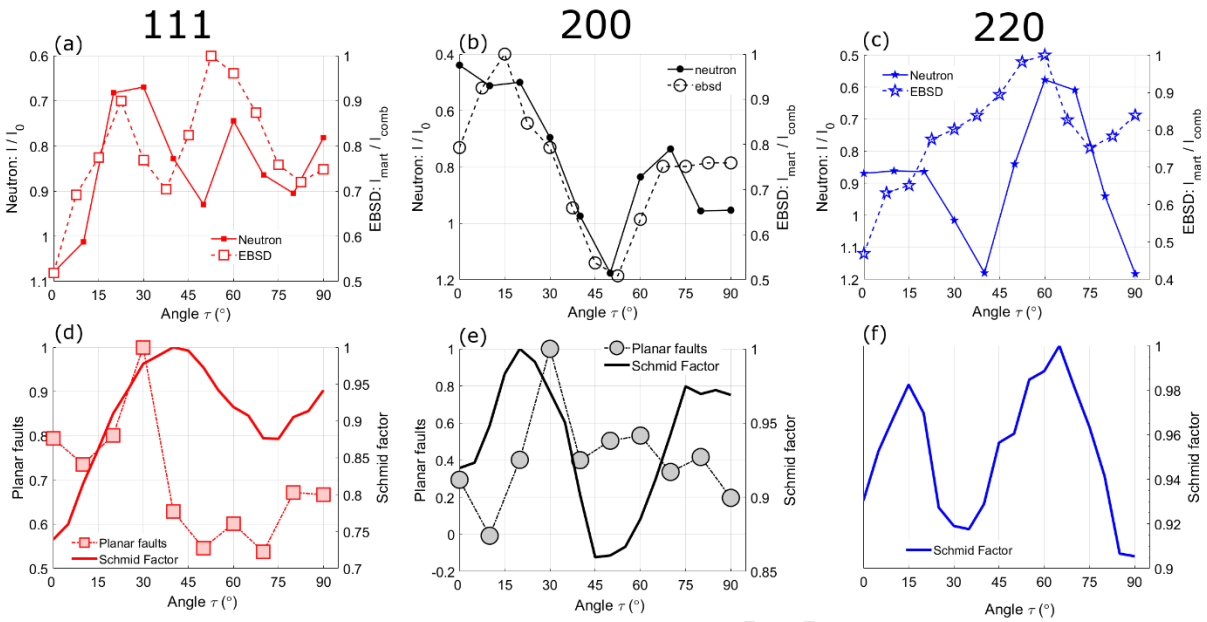

Figure 11.τ plots to indicate the amount of martensite formation (top subfigures a-c) and the amount of planar faults (bottom subfigures d-f). On the bottom subfigures (d-f) the Schmid factor is also shown. The values are shown for the 111 (a and d), 200 (b and e) and 220 (c and f) peaks. The values of martensite are determined by EBSD measurements at 10% strain (see

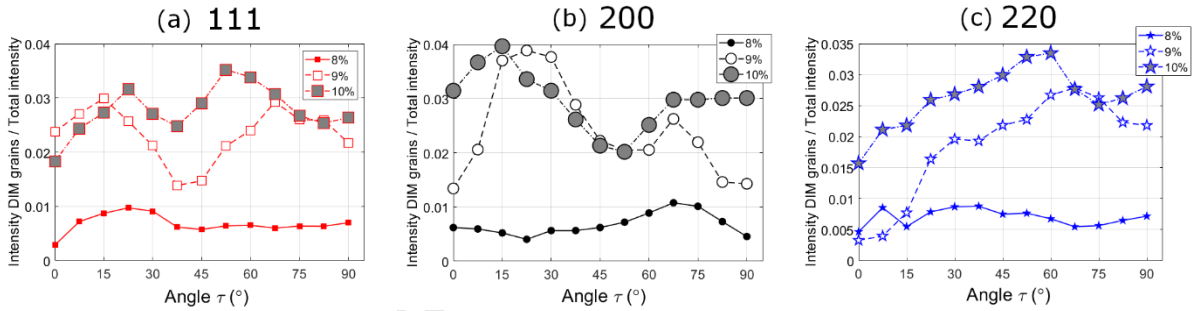

Figure 9), and the neutron measurements using Eq. 5 for SS316 values at 16% and SS301 values at 20% strain. The planar fault values are determined from lattice strains of SS301 at 20% strain using Eq. 3. Both planar faults and Schmid factor values are normalised relative to the maximum value.

5.2 Plastic Deformation

In Section 4.1 and Table 1 the relationship between the SEM measures of plastic deformation (KAM, BC, γ_{max}) and the Taylor and Schmid factors was discussed. It was found that, whereas there was a correlation, although weak, between the Taylor factor and the KAM and BC, the Schmid factor shows a correlation with γ_{max}. These observations are also found from the τ plots shown in Figure 12. The similarities between the Taylor factor and the values of the BC and KAM at 5% (a-c in the figure) include: (1) for the *111* peak a maximum at 0° then an fall to a minimum at ~40° followed by a fall, (2) for the *200* peak a maximum at ~50° and fall to lower values at 0° and 90°, (3) a fall from the values at 0° to 90°, for the KAM values the steep initial drop followed by a levelling off seen in the Taylor

factor is well matched. These trends with the Taylor factor and KAM and BC are more conclusive that the variables are correlated, than the weak correlations found in Table 1.

A relationship is often observed between the dislocation structure and the Taylor factor, whereby grains with higher Taylor factors have more developed dislocation cell structures [26,27], that is they are smaller with a greater misorientation across their boundaries. It may also be expected that grains with higher Taylor factors would have higher dislocation densities, although this is harder to verify. Hence, this would be consistent with a relationship being found between the BC and KAM with the Taylor factor. Since a more developed dislocation structure would be expected to cause more localised misorientation (KAM) and reduce the band contrast (BC).

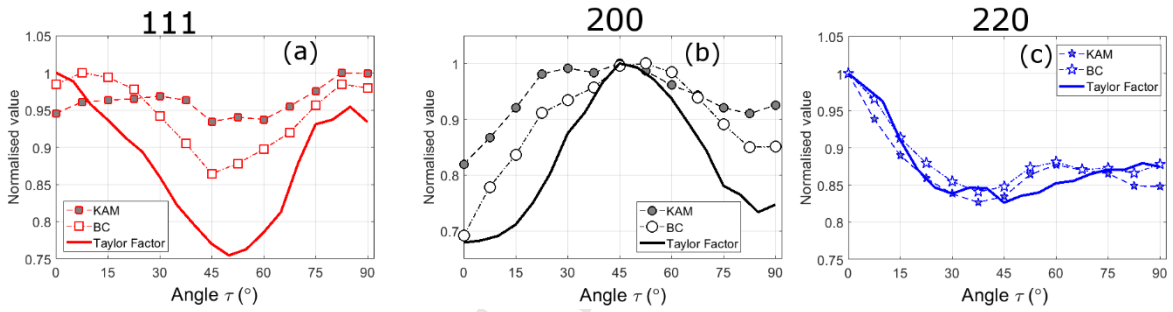

Figure 12. The change in KAM, band contrast and Taylor factor using the τ plots for (a) 111, (b) 200, (c) 220 peaks. The KAM and band contrast values are for SS301 samples after 10% applied strain.

The peak broadening of diffraction peaks can be directly related to the dislocation density, as shown in Eq. 1. However, to relate variations in broadening to changes in dislocation density is complicated because of differences in both the activity of different slip systems, which causes changes in the contrast factor, and differences in planar faults in different grains.

A similar procedure to that done with the neutron intensity data, in Figure 11, can be used with the broadening (full-width or FW) of the neutron data. That is by comparing the broadening of SS316 and SS301, to qualitatively determine the broadening due to the deformation induced martensite. If we say that:

$FW = FW_{slip} + Fw_{mart}$ and using: $FW_{mart} = 0$ for SS316.

The broadening due to the deformation induced martensite can be estimated as:

$$FW_{mart} = FW_{316} - FW_{301} \quad (6)$$

This is what is shown in Figure 13a-c. These changes share similarities to those found for the changes in martensite and planar faults shown in Figure 11. Most notably the maximum at τ ~30° for the *200* peak and the maximum at τ ~60° for the *220* peak. Hence, it appears that the difference in broadening between SS301 compared to SS316 is due to broadening by planar faults.

To investigate this further the additional broadening by planar faults, found from the lattice strains (Figure 6), are found using Eq. 2. This additional broadening is combined with the predicted broadening due to slip to give a predicted broadening caused by both slip and planar faults, as shown in Figure 13d-e. These additional predicted changes in broadening are comparable, in magnitude and angle τ, with the broadening observed for SS301. Most notably the unusual maximum for the *200* peak full-width at ~30° has an explanation as being caused by planar faults. Using this formula and the values of stacking fault percentage obtained from the lattice strains, the *111* peak is broadened by a maximum of 1 x 10^{-3} $Å^{-1}$ and *200* by 2 x 10^{-3} $Å^{-1}$. The contribution to the full-width from planar faults, from these calculations, is significant, being over half of the measured broadening of a peak. For a given fault percentage the broadening will be different for different *hkl* peaks. For example, a *111* peak will be broadened by 43% of the amount of a *200* peak, whilst the *220* peak will be broadened by 71% of the *200* peak's value. These differences may partly explain why the full-width differences are much smaller for the 111 peak than the others.

Although, interpretation of the broadening changes on the τ plots is more ambiguous than the other changes observed. It does provide secondary verification to the planar fault changes found using the lattice strains, and of a link between the Schmid factor and the formation of planar faults in different orientations.

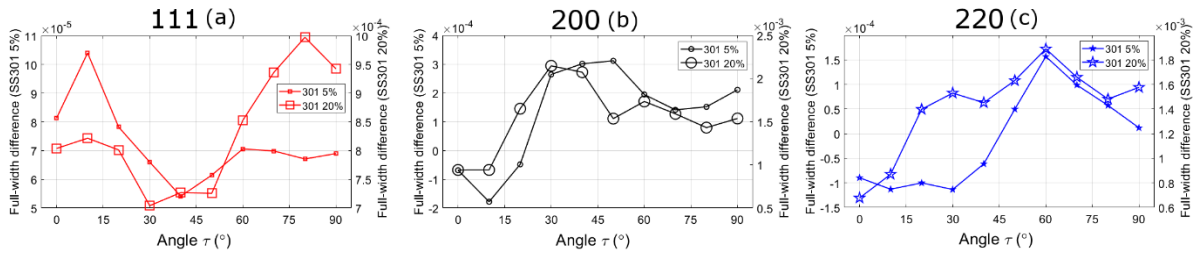

Figure 13. The difference in full-width between SS301 and SS316 for (a) 111, (b) 200, and (c) 220 peaks. The values for SS301 at 20% applied strain are shown and compared with SS316 at 16% applied strain. The broadening of SS301 at 20% applied strain is shown in (d-e) for 111 and 200 peaks. In these plots are predicted changes based only on slip activity and slip activity and planar faults. Where the planar fault values found using the lattice strains are used. In d-e the values are normalised relative to the broadening of the 311 peak.

5.3 Averaging considerations

The orientation of a grain can be represented in several ways, one of the most popular ways in materials science is by three scalar values known as Euler angles [32]. However, it is not possible to define orientation uniquely by one or even two scalar values. Hence why for interpreting texture (or preferred orientation) changes, pole and inverse pole figure plots are used. In addition to this issue, there is also the problem that even grains with the same orientation can behave differently given the surrounding grains. These issues make it difficult to quantify and understand the heterogeneity of a sample in a concise way.

One way around this, and to investigate the behaviour of a grain given its orientation, is by comparing it to a known variable, such as the Taylor or Schmid factor as shown in Table 1. However, this is of little use when we don't know the variable that governs the changes, we want to investigate a transition between variables, or we want to quantify how different orientations behave. Hence, some sort of averaging procedure is needed to understand the heterogeneity of deformation. The approach presented in this work is essentially an averaging procedure over grains of different orientations along the same lines done with texture measurements using the pole figure plot. It is therefore worth considering the implications of the averaging involved within these τ plots, some of which are highlighted in Figure 14.

As explained in Section 3.4, EBSD measurements are obtained for different τ values at distinct angles between the tensile direction and the diffraction vector, however these are not across a single rotation axis as is done by powder diffraction measurements (e.g. between the y-axis and the z-axis in Figure 1). Hence, it would be expected that the

percentage of grains contributing to a given peak would increase with increasing τ for EBSD measurements. Which is what is found as shown in Figure 14, where at τ =0° less than 5% of grains contribute to a measurement, whilst at τ =90° around 25% of grains contribute to a measurement with the *111* and *200* peaks. A given grain can contribute to several measurement angles on the τ plot of a given peak, because there are multiple equivalent planes. For example, for the *200* peak/plane there are six planes (*200*, *020*, *002* and their negatives) representing the outer planes of the unit cell. For the *111* and the *220* planes there are more equivalent planes. This is why the percentage of contributing grains can be so high, being 50% for the *220* peak at τ =90°. For powder diffraction measurements the amount of contributing grains would be dependent on the texture and would be more constant with angle. Since a given measurement point on a τ plot will be due to the contributions of many grains, there will be a variation of values for each τ plot point. To investigate these variations the standard deviation of selected variables determined by polycrystal plasticity models are shown in the τ plots of Figure 14b-d.

In Figure 14c-d are changes in the standard deviation of the Taylor factor and Schmid factor using the τ plots. The values here are obtained between the y-axis and the z-axis, but similar changes and magnitudes are obtained if the values are obtained in the same way as the EBSD values are obtained. Whilst the standard deviation in the Schmid factor oscillates with increasing τ for the peaks, for the Taylor factor the standard deviation increases with τ for all peaks. The magnitude of the standard deviation of the Schmid factor is ~0.04. This value is significant given that it is approximately 10% of the average Schmid factor values, or approximately the same magnitude as the difference between maximum and minimum Schmid factor values of a given peak. The magnitude of the standard deviation of the Taylor factor is similar in relative magnitude, being ~10% of the average Taylor factor values. If we are to assume that the deformation microstructure is governed by a combination of the Taylor and Schmid factors, then there will be a greater uncertainty of defining this with increasing τ. However, this may be countered somewhat by the increase in contributing grains with increasing τ, which could reduce this uncertainty.

The standard deviation in lattice strain obtained by CPFEM modelling is shown in Figure 14b. The values increase significantly towards τ =90° for the *200* peak, but for the other peaks it is approximately constant with τ and increases only slightly between 0° and 90° for *111* and

220 peaks. The standard deviations are significant, being of a similar magnitude to the absolute lattice strain values shown in Figure 6. In research that uses the lattice strains to model the plastic deformation of a sample, measurements are most often taken at τ angles of 0° and 90°. In these works, there can be problems with modelling the changes of lattice strain at τ =90° [2,33], which is often explained as being due to the variation in the lattice strain at this angle. However, it could instead be an issue with the models themselves. Some of the uncertainty surrounding the modelling of lattice strain may be reduced by taking measurements at angles between the axial (τ =0°) and transverse (90°) directions. This is because at intermediate angles the standard deviation is as small as in the axial direction, but the lattice strains are significantly different to the axial and transverse directions. For example, for each of the peaks the lattice strain at an angle of τ ~ 45° is most different to the lattice strain in the axial direction whilst the standard deviation is approximately the same as the axial direction. Although it may not be practical to do these additional measurements during loading, it is relatively easy to perform a range of τ values measurements after unloading to enhance any lattice strain modelling measurements. Measurements at a range of τ angles as shown here would also be advantageous as more of the grains in a sample are being sampled, whilst changes in lattice strain with τ can be investigated.

Given these limitations, particularly the high values of standard deviation relative to the absolute values, it is interesting to note that the τ plot results presented have shown clear trends that also follow results of polycrystal plasticity models.

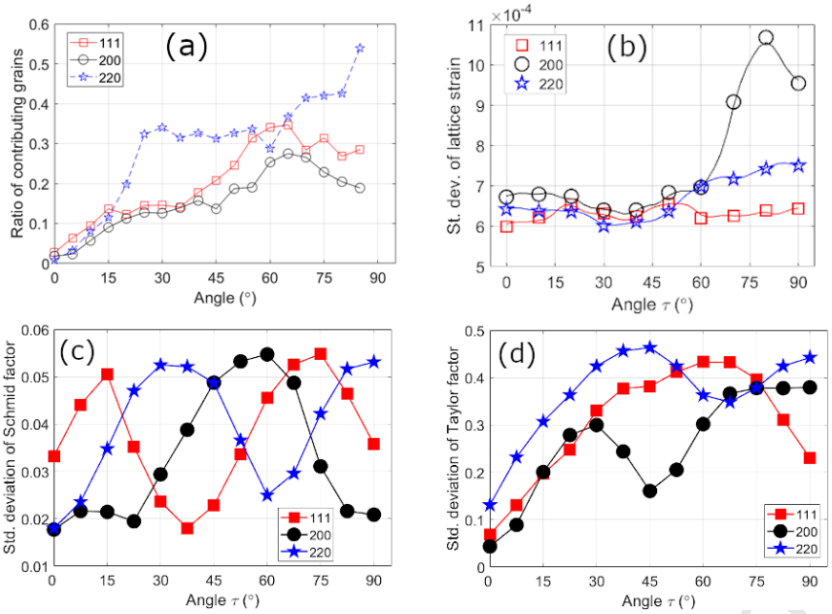

Figure 14. In (a) are the ratio of contributing grains to EBSD measurements, in (b) the standard deviation of lattice strains determined by a CPFEM model, in (c) the standard deviation of the Schmid factor, and (d) the standard deviation of the Taylor factor. All subfigures are at different angles τ for peaks 111, 200 and 220.

6 Conclusions

The results and discussion presented here show that the τ plot approach allows multi-scale characterisation of the heterogeneous plastic deformation in crystalline materials. It has been able to highlight and quantify the significant heterogeneity in the plastic of deformation of stainless steel alloys. The approach can be used with either powder diffraction or SEM based experiments, or a combination of both.

For powder diffraction, the τ plot approach allows information about several parameters to be obtained in a single experiment, which can then be compared or modelled to give information about the deformation heterogeneity. The parameters include: lattice strains, texture evolution, peak broadening and planar fault percentage. If only axial and transverse measurements are made it would be difficult to relate the changes in these properties in a significant way, and many of the interesting changes that occur between these two angles would be missed. For example, in this work the main changes in martensite and planar faults were found at τ angles of around 45°. Furthermore, changes in lattice strain, intensity and peak broadening were linked. This enabled us to show a correlation between the amount of martensite formed in a grain and the planar faults present, and that these changes were correlated to the Schmid factor. In addition, measurements like this may also

offer greater insight into the discrepancy often found in models to explain lattice strains in the transverse direction.

For SEM measurements, the τ plot approach provides an averaging procedure that enables us to understand and model deformation heterogeneity. This averaging procedure is beneficial to understand deformation heterogeneity due to the stochastic nature of plastic deformation and because several scalar quantities are needed to define a crystal's orientation. The τ plot approach allows us to quantify and compare systematic changes in the microstructural quantities obtained by SEM measurements. For example, in this work a correlation between the amount of plastic deformation of a grain, through the band contrast and kernel average misorientation, and its Taylor factor has been shown. Whilst, the surface strain from DIC and the martensite formation are correlated with the Schmid factor.

For use with both powder diffraction and SEM measurements, the τ plot approach provides a way to combine measurements from the two techniques. The two techniques are complementary with both the information they provide and how the techniques work. Some information can be directly related in the two techniques, such as preferred orientation, some are related, such as full-width from powder diffraction and the band contrast and kernel average misorientation from SEM, and some that are not available in the other technique, such as lattice strains from powder diffraction and microstructural details such as grain size or surface strain from SEM. In addition, whilst neutron diffraction provides information from a much large volume of the sample than by SEM measurements, it does not provide the local microstructural information provided by SEM measurements. The combination of the two techniques therefore allows for a more detailed characterisation of a sample due to the utilisation of the strengths of both. For example, the reason for changes in intensity measured by powder diffraction can be interpreted from the microstructural changes observed from EBSD measurements, as was done here with martensite formation. Whilst the changes of full-width can be interpreted as a combination of multiple factors, and not given by the dislocation and sub-grain size alone

Acknowledgements

The authors are grateful to the UK Science and Technology Facilities Council for the beam time granted at the ISIS facility (HRPD beamline). THS's contribution was part funded by the European Regional Development Fund as part of the Ser Cymru II program. MEF is grateful for funding from the Lloyd's Register Foundation, a charitable foundation helping to protect life and property by supporting engineering-related education, public engagement and the application of research. JQF acknowledges funding from the EPSRC programme grant Lightform (EP/R001715/1).

References

[1] Y.B. Das, A.N. Forsey, J. Kelleher, S. Kabra, M.E. Fitzpatrick, T.H. Simm, S. Gungor, R.J. Moat, Mater. Sci. Technol. 0836 (2018) 1–12.

[2] J. Quinta da Fonseca, E.C. Oliver, P.S. Bate, P.J. Withers, Mater. Sci. Eng. A. 437 (2006) 26–32.

[3] B.E. Warren, X-Ray Diffraction, Addison-Wesley Publishing Co., Reading, 1969.

[4] T. Simm, Crystals. 8 (2018) 212.

[5] T.H. Simm, P.J. Withers, J. Quinta da Fonseca, Mater. Des. 111 (2016) 331–343.

[6] P.S. Bate, J. Quinta da Fonseca, Mater. Sci. Eng. A. 380 (2004) 365–377.

[7] Y.B. Das, A.N. Forsey, T.H. Simm, K.M. Perkins, M.E. Fitzpatrick, S. Gungor, R.J. Moat, Mater. Des. 112 (2016).

[8] S. Birosca, G. Liu, R. Ding, J. Jiang, T. Simm, C. Deen, M. Whittaker, Int. J. Plast. (2019).

[9] A.N. Forsey, Y.B. Das, T.H. Simm, D. Clarke, J. Boswell, S. Gungor, R.J. Moat, Mater. Sci. Eng. A. 712 (2018) 681–684.

[10] H. Lim, J.D. Carroll, C.C. Battaile, T.E. Buchheit, B.L. Boyce, C.R. Weinberger, Int. J. Plast. 60 (2014) 1–18.

[11] Y. Tian, O.I. Gorbatov, A. Borgenstam, A. V. Ruban, P. Hedström, Metall. Mater. Trans. A Phys. Metall. Mater. Sci. 48 (2017) 1–7.

[12] A. Das, S. Tarafder, P.C. Chakraborti, Mater. Sci. Eng. A. 529 (2011) 9–20.

[13] T.H. Simm, The Use of Diffraction Peak Profile Analysis in Studying the Plastic Deformation of Metals, PhD thesis, University of Manchester, 2012.

[14] T.H. Simm, P.J. Withers, J. Quinta da Fonseca, J. Appl. Crystallogr. 47 (2014) 1535–1551.

[15] Y.B. Das, PhD thesis, The Open University, 2017.

[16] DaVis, LaVision, GmbH, Goettingen, 2016.

[17] T.H. Simm, A. Forsey, (2016). www.dMata.co.uk/dbsd_dice.

[18] F. Bachmann, R. Hielscher, H. Schaeben, Ultramicroscopy. 111 (2011) 1720–1733.

[19] G. Kurdjumov, G. Sachs, Z. Phys. 64 (1930) 325–343.

[20] G.. Williamson, W.. Hall, Acta Metall. 1 (1953) 22–31.

[21] M. Wilkens, Fundamental Aspects of Dislocation Theory, Vol. II, Natl. Bur. Stand. (US)Spec. Publ. No. 317, Washington DC USA, 1970.

[22] A. Borbély, J. Dragomir-Cernatescu, G. Ribárik, T. Ungár, A. Borbely, J. Dragomir-Cernatescu, G. Ribarik, T. Ungar, J. Appl. Crystallogr. 36 (2003) 160–162.

[23] P. Bate, Philos. Trans. R. Soc. A Math. Phys. Eng. Sci. 357 (1999) 1589–1601.

[24] G. Kendall, M., A. Stuart, The Advanced Theory of Statistics, 4th edn, New York, 1979.

[25] J.D. Evans, Straightforward statistics for the behavioral sciences, Brooks/Cole Pub. Co., Pacific Grove, 1996.

[26] I.L. Dillamore, P.L. Morris, C.J.E. Smith, W.B. Hutchinson, G. V Raynor, Proc. R. Soc. London. A. Math. Phys. Sci. 329 (1972) 405–420.

[27] N. Hansen, X. Huang, W. Pantleon, G. Winther, Philos. Mag. 86 (2006) 3981–3994.

[28] G. Guiglionda, A. Borb, J.H. Driver, Acta Mater. 52 (2004) 3413–3423.

[29] A. Borbely, J.H. Driver, T. Ungár, Acta Mater. 48 (2000) 2005–2016.

[30] G.I. Taylor, Proc. R. Soc. A Math. Phys. Eng. Sci. 145 (1934) 362–387.

[31] G. Sachs, Z. Ver. Deu. Ing. 72 (1928) 734.

[32] O. Engler, V. Randle, Macrotexture Analysis, in: Introd. to Texture Anal., CRC Press, 2009: pp. 73–73.

[33] C.J. Neil, J.A. Wollmershauser, B. Clausen, C.N. Tomé, S.R. Agnew, Int. J. Plast. 26 (2010) 1772–1791.

Appendix A

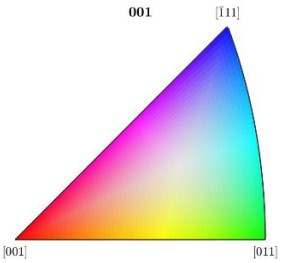

Figure A1. The inverse pole figure colour notation for the following figures. The external direction used is out of the surface, perpendicular to the applied load (which is in the horizontal x-direction.

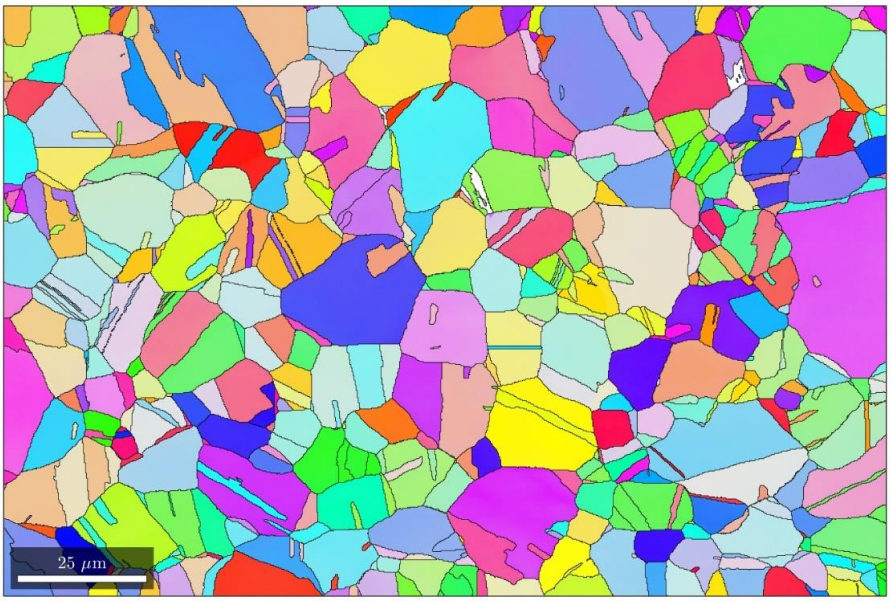

Figure A2. Starting EBSD orientation map used for the DIC in situ data analysis presented of SS301.

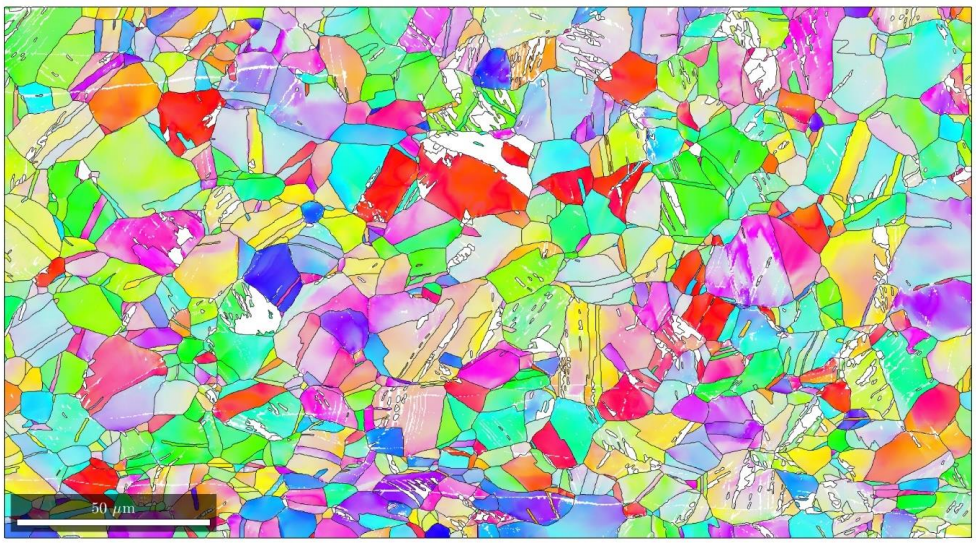

Figure A3. Typical EBSD orientation map used for the ex situ data analysis presented of SS301. In this case the sample is deformed to 10% applied strain.

Appendix B

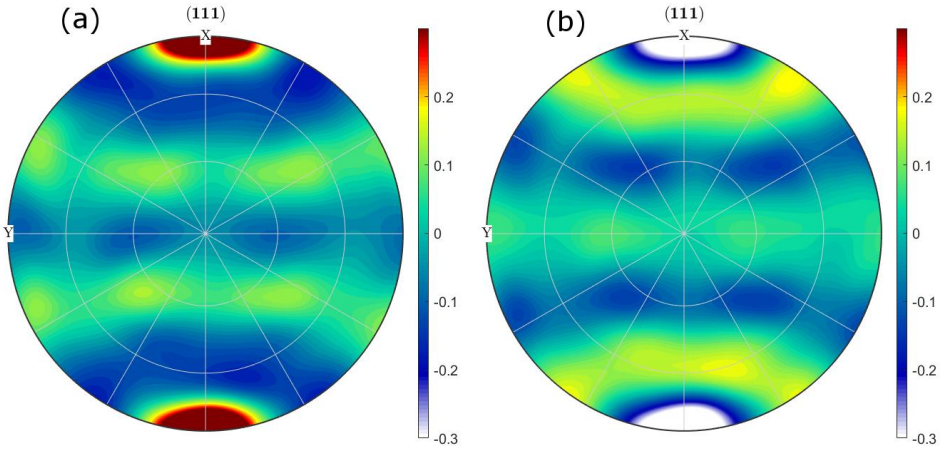

Figure B1. 111 pole figures from Taylor model calculations after a strain of 10%. The figure shows the difference between final and starting intensity, for (a) tension and (b) compression. Where x is the tensile/compression direction.

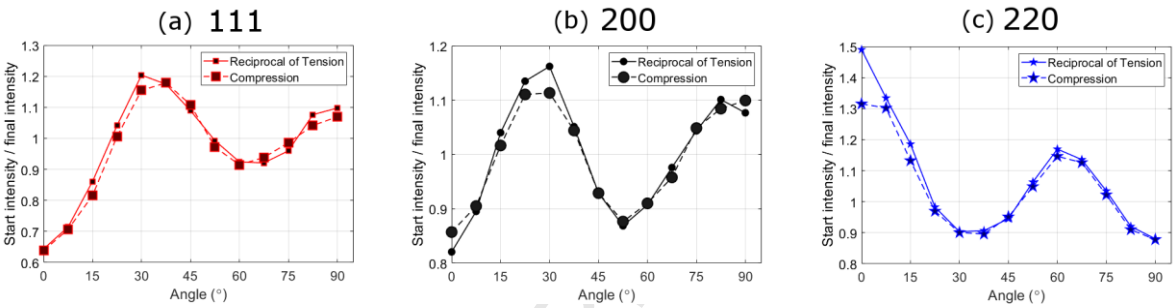

Figure B2. τ plots for 111, 200 and 220 peaks using Taylor model calculations after a strain of 10%. The figure shows the ratio of final and starting intensity for compression test and the reciprocal of this for tension test.

Appendix C

Table C1. The Pearson correlation coefficient for the grain averaged values of different variables. The data is for SS301 after 9% applied strain, the DIC data uses a higher magnification (and lower area) map than the BC and KAM data. For the band contrast values, its reciprocal is used. The DIC data uses the high magnification map.

	DIC	KAM	BC	TF	SF
DIC	-				
KAM		-			
BC		0.54	-		
TF	-0.29	0.14	0.26	-	
SF	0.70	-0.02	-0.22	-0.64	-

Table C2. The Pearson correlation coefficient for the grain averaged values of different variables. The data is for SS301 after 8% applied strain, the DIC data uses a higher magnification (and lower area) map than the BC and KAM data. For the band contrast values, its reciprocal is used. The DIC data uses the high magnification map.

	DIC	KAM	BC	TF	SF
DIC	-				

KAM		-			
BC		0.49	-		
TF	-0.19	0.08	0.22	-	
SF	0.68	0.06	-0.18	-0.56	-

Appendix D

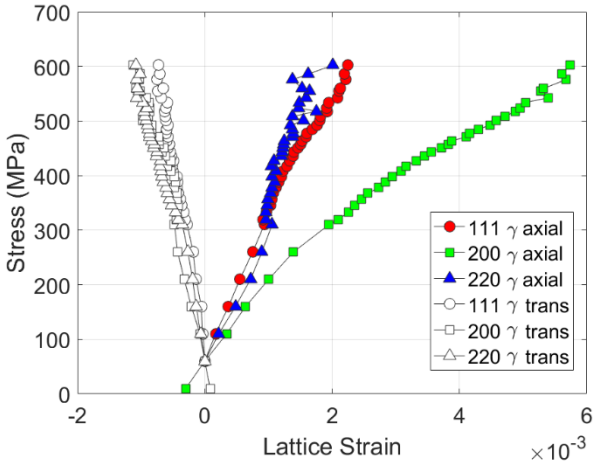

Figure D1. Lattice strain against stress for SS301 deformed at room temperature measured at ENGIN-X. See [6] for details of the experimental setup.

Conflict of interests
There are no conflict of interests

Highlights

An approach is presented that allows multi-scale characterisations of heterogeneous deformation in crystalline materials by employing a range of characterisation techniques including: electron backscatter diffraction, digital image correlation and neutron diffraction powder measurements. The approach will be used to obtain critical information about the variations in parameters that characterise the deformed state in different crystallographic orientation texture components of a sample in a statistically significant way. These parameters include lattice strains, texture evolution, peak broadening, dislocation density, planar faults, phase changes and surface strain. This approach allows verification of models of plastic deformation to provide a more detailed view of plastic deformation heterogeneity at multiple length scales than obtained by other characterisation approaches. The approach demonstrated here is applied to two stainless steel alloys; an alloy that exhibits phase transformation during deformation and an alloy that remains the same phase all through deformation process.